

The Geochronology and Structural
Evolution of the Warren Inlier and
Springfield Sequence, Mt. Lofty
Ranges: Implications for Proterozoic
Paleogeographic Reconstructions.

Thesis submitted in accordance with the requirements of the University of
Adelaide for an Honours Degree in Geology

Kieran Meaney

November 2012



THE UNIVERSITY
of ADELAIDE

ABSTRACT

The Warren Inlier is one of five Paleoproterozoic inliers in the Mt. Lofty ranges and represents the easternmost exposure of the Gawler Craton. This inlier is dominated by a Mesoproterozoic S_2 fabric which was later deformed in a dominantly E-W to NE-SW stress regime during the Delamerian Orogeny. Regional scale fold orientations indicate that this fabric was near horizontal prior to the Delamerian deformation. Metamorphic monazite and zircon from early pegmatites suggest that this fabric formed at approximately 1570 – 1560 Ma. A metamorphic event is also recorded in the Springfield Sequence at ~ 1580 Ma, which is consistent with previous studies in the Barossa Complex, and is coincident with the Olarian Orogeny in the Curnamona Province to the east. The younger ~1560 Ma ages are consistent with a retrograde metamorphic event also documented in the Curnamona Province, and it is likely that these regions share this tectonic history.

The Springfield Sequence to the immediate east of the Warren Inlier has been shown to be an allochthonous basement unit, as opposed to sheared Adelaidean metasediments as they were originally mapped. Detrital zircons from this sequence indicate that deposition of this part of the basement occurred between 1744 Ma and 1625 Ma. This indicates that the Barossa Complex was deposited after the Wallaroo Group to the west, and prior or synchronous to the lower Willyama supergroup. This may be representing a western extension of the Willyama Supergroup, or potentially a progressive eastward stepping series of basins was developing on the eastern margin of the Gawler Craton between 1800 Ma and 1600 Ma, which may in turn be an indication of a retreating subduction margin.

KEYWORDS

Structural geology, Geochronology, Zircon, Monazite, Gawler Craton, Paleoproterozoic, Mesoproterozoic, Nuna

TABLE OF CONTENTS

Abstract	1
Keywords	2
List of Figures and Tables.....	4
1. Introduction.....	6
2. Geological Setting.....	7
3. Methods.....	9
4. observations and Results.....	11
4.1 The Warren inlier.....	11
4.1.1 - Lithology	11
4.1.2 - Structure.....	16
4.1.3 - Geochronology	20
4.2 – The Springfield Sequence	24
4.2.1 – Lithology.....	24
4.2.2 – Structure	25
4.2.3 – Geochronology.....	26
4.2.4 - Th/U Ratios	26
5. Discussion	29
5.1 Interpretation of geochronological data	29
5.2 Structural evolution of the Warren Inlier and Springfield Sequence.....	31
5.3 Implications of this study.....	34
6. Conclusions.....	38
Acknowledgments.....	39

LIST OF FIGURES AND TABLES

Figure 1: Geology of the Mt. Lofty Ranges, South Australia, and inset, positions of the Gawler Craton and Curnamona Province (CP) in South Australia.....	7
Figure 2: Structural geology map of the Warren Inlier. Note: Grey data represents that presented by Mills (1973)	14
Figure 3: a) Structurally mature pegmatite showing a strong internal fabric which has been subsequently deformed. b) Younger generation of pegmatite which is folded with no internal fabric. c) S_2 schistosity fabric overprinting the early pegmatite. d) Disharmonic folds in Warren Gneiss. e) Outcrop scale folds in the Spillway Type Section. f) Photomicrograph of relict S_1 fabric being overprinted by the dominant S_2 fabric.	15
Figure 4: a) Outcrop map of the Spillway Type Section. b) Poles to S_2 fabric showing distribution along a NE-SW profile plane (n=123). c) Poles to F_3 axial planes (black squares, n=35) and F_3 fold hinge lineations (red triangles, n=23). Axial planes show a spread along a NE-SW profile plane. d) Poles to F_3 crenulations (black squares, n=11) and F_3 crenulation hinge lineations (red triangles, n=9). Crenulation axial planes show distribution along a NE-SW profile plane. e) Major F_4 fold axial planes (n=3) which are axial planar to earlier trends. These data demonstrates the coaxial nature of the D_3 and D_4 phases, suggesting that they may represent the same progressive deformation phase.....	16
Figure 5: Equal area stereonet plots of poles to S_2 schistosity. The northwest area shows a spread of S_2 poles that spread around an east to West profile plane, indicating north-south trending fold axes (n=32). The northeast area shows a spread of S_2 poles depicting a best fit profile plane striking NE-SW, indicating northwest-southeast trending fold axes (n=33). The Southern area displays less discernable trends when broken into subareas, and is presented as one area. This area shows a weak S_2 spread from ENE-WSW, which is likely a reflection of interference from the two recognised orientations seen in the north (n=65).	17
Figure 6 (Left): Sketch of outcrop in Spillway Type Section showing F_3 folds coaxially refolded around the F_4 axis	19
Figure 7 (Left): a) Density contours of poles to F_3 axial planes, showing clusters of upright roughly N-S striking fold axial planes, which show a spread around an ENE-WSW plane. b) F_3 fold hinge lineations which show a SE clustering. c) F_4 poles to crenulation axial planes showing a distinct e-w clusters but with significant spread to the NE, possibly due to D_4 or a later e-w trending fold phase. d) F_4 crenulation hinge lineations showing clustering to the south.....	19
Figure 8: CL and BSE images of analysed zircon and monazite grains. a) BSE images of monazites from sample KM12-05. b) BSE images of monazite grains from sample KM12-08. c) CL images of zircon grains from sample KM12-01 showing inherited cores and oscillatory zoning in magmatic rims. d) CL images of zircon grains from sample KM12-07. Zoning is obscured by dark colouration. e) CL images of detrital zircon grains from sample KM12-17. f) CL images of metamorphic zircons from sample KM12-11.....	20
Figure 9: Concordia plots for monazite analyses from KM12-05. Top – all data, bottom – blow up of red square in the top plot, showing the younger population.....	21
Figure 10: Concordia plots of monazite analyses from KM12-08. Top – All data. Bottom – Blow up of the red square in the top figure, showing the older population.....	22
Figure 11: Concordia plot of zircon analyses from sample KM12-01	23
Figure 12: Concordia plot of zircon analyses from sample KM12-07	23
Figure 13: Equal area stereonet projections of measurements from the Springfield Shear Zone. a) Poles to schistosity planes showing minor spreading along a NE-SW trending axis. b) Poles to crenulation axial planes, showing clustering to the west. c) Crenulation hinge	

lineations, showing minor spreading along a NNW-SSE trending axis. d) Mineral streaking lineations showing minor spreading along a NW-SE trending axis	25
Figure 14: Concordia plot of zircon analyses from sample KM12-11	26
Figure 15: Top - Concordia plot of zircon analyses from sample KM12-17, and, Bottom - probability density diagram of detrital zircon ages.....	27
Figure 16: Th/U ratio vs. Pb^{207}/Pb^{206} ages plots for samples KM12-11 (top) and KM12-17 (bottom).....	28
Figure 17: Block diagram of the northern Warren Inlier showing open, upright, symmetrical regional fold orientations, which continue into the Burra Group cover sequence. Cross section line A-B as marked on Figure 2.	33
Figure 18: field sketch of angular unconformity from Mills (1973, Figure 3f). From left: Burra group displaying Delamerian S_1 schistosity, bedding described by heavy mineral laminations (light grey), and irregular contact horizon with the Warren Gneiss (dark grey) displaying S_2 fabric. Note angle between Burra group S_1 and Warren Gneiss S_2	34
Figure 19: Detrital spectra for the Willyama Supergroup after Barovich & Hand (2008). The Lower Willyama Supergroup (dark line) displays peaks at ~1700 and 1800 Ma, with minor peaks at ~2300 and 2600 Ma	36

1. INTRODUCTION

The Neoproterozoic – Proterozoic Gawler Craton and Curnamona Province of South Australia and western New South Wales (Figure 1) are often included in paleogeographic reconstructions (e.g. Giles *et al.* 2004, Betts & Giles 2006, Wade *et al.* 2006, Rutherford *et al.* 2007, Betts *et al.* 2008, Payne *et al.* 2009, Boger 2011). This is because the region contains voluminous Proterozoic magmatism and extensive coeval sedimentary basins punctuated by a series of tectothermal events (e.g. Hand *et al.* 2007) that suggest the region lay on a plate margin throughout this time. However, a recent paleomagnetically constrained reconstruction of the geography of these times (Zhang *et al.* 2012) places Australia in the centre of the supercontinent Nuna (Also known as Columbia; e.g. Zhao *et al.* 2004, Meert 2012) from ~1740 – 1400 Ma. To geologically question this reconstruction a better understanding of the nature of the tectonism in the Gawler Craton and Curnamona Province is required. In this study, a start is made towards this by examining the history and timing of crust formation in the Barossa Complex, the basement to the Adelaide Rift Complex between the Gawler Craton and Curnamona Province.

The Barossa Complex (Figure 1) is the easternmost exposure of the Gawler Craton and is exposed as basement inliers within the Mt. Lofty ranges, South Australia (Preiss 1993). However, despite being in close proximity to Adelaide, this complex remains largely unstudied and poorly understood. As the south-eastern most exposure of the Gawler Craton, the Barossa Complex represents a valuable opportunity to study the eastern margin of the craton (Szpunar *et al.* 2007). In this study a structural map of the Warren Inlier and part of the adjacent Springfield Sequence is presented, along with new U-Pb ages from metamorphic monazite grains and igneous zircon grains from pegmatites in order to constrain the timing of metamorphic and tectonic events. Detrital and metamorphic zircon ages are also presented from metasedimentary rocks from the Springfield Sequence in order to test whether this zone

is part of the Barossa Complex, and if so, to provide constraints on depositional timing of the protoliths to the Barossa Complex.

2. GEOLOGICAL SETTING

The Barossa Complex consists of five Paleoproterozoic inliers, the Houghton, Warren, Aldgate, Oakbank, and Myponga Inliers, located within the Mt. Lofty ranges of South Australia (Figure 1) (Preiss 1993). These inliers extend from near Williamstown, approximately 50 km north-east of Adelaide, to the Normanville area 70 km south of Adelaide, and vary in size from 5 km² to 100 km² (Szpunar *et al.* 2007). The Barossa Complex is unconformably overlain by the Neoproterozoic to Cambrian sediments of the Adelaide Rift Complex (Preiss 2000). This

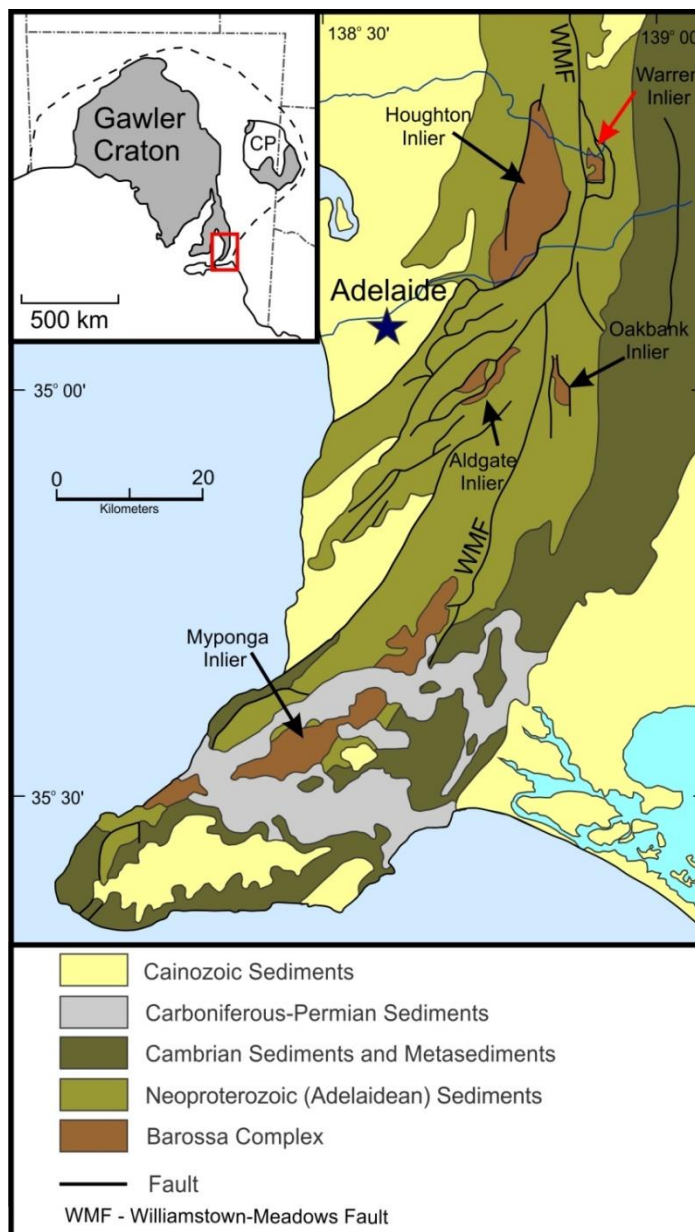


Figure 1: Geology of the Mt. Lofty Ranges, South Australia, and inset, positions of the Gawler Craton and Curnamona Province (CP) in South Australia.

sequence was regionally deformed and metamorphosed by the multiphase Cambro-Ordovician Delamerian Orogeny (Offler & Fleming 1968, Mancktelow 1990) between 514 Ma to 490 Ma (Foden *et al.* 2006). The Adelaidean sequence was variably deformed during this event, with a lower grade biotite zone to the east of the Williamstown-Meadows fault

dominated by recumbant to isoclinal D₁ folds, while a higher grade sillimanite zone to the east shows stronger overprinting of D₂ and D₃ structures (Offler & Fleming 1968, Mancktelow 1990).

The inliers comprising the Barossa Complex (Figure 1) are composed of poly-deformed metasedimentary and metagneous rocks, which have experienced amphibolites to granulite facies metamorphism, as well as two retrograde metamorphic events (Talbot 1963, Mills 1973). However, aside from the Delamerian Orogeny (514 - 490 Ma, Foden *et al.* 2006) the specific timing and setting of these events is still largely unknown, and any preserved pre-Delamerian structure is poorly described.

Previous geochronological studies of the Barossa Complex have been focussed on the two largest inliers; the Houghton Inlier and the Myponga Inlier. A study of modern stream sediments in the Houghton Inlier led Belousova *et al.* (2006) to identify a magmatic event at 1718 ± 8 Ma, and a consequent metamorphic event at 1625 ± 9 Ma. Due to the nature of this study, stratigraphic significance of these ages could not be definitively constrained, however it was assumed that the magmatic age represents the crystallisation of a large body of orthogneiss outcropping in the Houghton Inlier. Whether the granite protolith to this gneiss was a synsedimentary intrusion or synorogenic intrusion is unknown, although the timing of crystallisation is within the known range of the ca. 1730 – 1690 Ma Kimban orogeny (Hand *et al.* 2007).

In the Myponga Inlier, Crowhurst (1988) identified two deformation phases which were cross cut by an aplite intrusion at 1577 ± 22 Ma, and it is possible that the ages presented by Belousova *et al.* (2006) represent these two earlier deformation events, however without further study this is highly speculative. Preiss (1993) and Szpunar *et al.* (2007) have reported ages for igneous and metamorphic events in the Houghton and Myponga Inliers at approximately 1590 Ma, which corresponds temporally to the ca. 1600 – 1580 Ma Olarian

Orogeny in the Curnamona Province (Raetz *et al.* 2002, Rutherford *et al.* 2007) and the intrusion of the Hiltaba Suite granites (e.g. Creaser & Cooper 1993, Flint *et al.* 1993).

Early work by Cooper & Compston (1971) obtained a whole rock Rb-Sr isochron of 867 ± 32 Ma for the Houghton Inlier. To date, the only published age within error of this age are granitic intrusions in the Oakbank Inlier at 856 ± 20 Ma, which have been interpreted as being related to the early continental rift phase which formed the basin in which the Adelaidean sequences were deposited (Preiss *et al.* 2008).

The Warren Inlier lies within the high grade (sillimanite) zone of the Delamerian orogen (Mancktelow 1990), and is overlain by basal grits of the Burra group (Mills 1973). The area surrounding the Warren Inlier was mapped in detail by Mills (1973), however the structure of the basement was poorly described, and no further study has been done on the Warren Inlier. The area mapped as the Springfield Shear Zone to the immediate east of the Warren Inlier is also host to a granite gneiss (Mills 1963). This gneiss has been dated by Preiss *et al.* (2008) at 812 ± 6 Ma, which is also interpreted to have intruded during the Adelaidean rifting. Before this age was identified, the Springfield Shear Zone was mapped as Adelaidean metasediments (Mills 1973, Ringenbergs 1975), however an allochthonous basement unit is now more likely (Preiss *et al.* 2008). Because of this, the Springfield Shear Zone will be herein referred to as the Springfield Sequence, as to avoid any genetic connotations.

3. METHODS

Structural mapping of the Warren Inlier was undertaken to build upon the structural map of Mills (1973). Structural data were analysed using the Stereonet 7 software (Allmendinger *et al.* 2012). Samples were collected from the Warren Inlier and the Springfield Sequence for zircon and monazite U-Pb geochronological analysis.

Zircon and monazite grains were separated from samples using standard crushing, panning, Franz magnetic, and heavy liquid separation techniques. Zircon and monazite grains were imaged using Backscatter Secondary Electron (BSE) and Cathodoluminescence (CL) imaging on a Phillips XL-20 SEM with attached Gatan CL detector. Single-grain U–Pb zircon dating was undertaken using Laser Ablation Inductively Coupled Plasma Mass Spectrometry (LA-ICP-MS) at the Adelaide Microscopy. U–Pb isotopic analyses were obtained using a NewWave 213 nm Nd-YAG laser in a He ablation atmosphere, coupled to an Agilent 7500cs ICP-MS. A 60 second gas blank was analysed followed by 60 seconds of measurement during zircon ablation. For monazite analyses, a 50 second blank and 50 seconds during ablation were analysed. Prior to each ablation the laser is fired for 10 seconds with the shutter closed to allow crystal and beam stabilisation.

For the zircon analyses, the zircon standard GEMOC GJ-1 (TIMS normalisation data: $^{207}\text{Pb}/^{206}\text{Pb} = 608.3 \text{ Ma}$, $^{206}\text{Pb}/^{238}\text{U} = 600.7 \text{ Ma}$ and $^{207}\text{Pb}/^{235}\text{U} = 602.2 \text{ Ma}$) was used as a matrix-matched standard to correct for mass bias and fractionation (Jackson *et al.* 2004). Accuracy was checked using the Sri Lankan in house standard BJWP (ca. 727 ma) and the recognised zircon standards Plesovice ($337.13 \pm 0.37 \text{ Ma}$, Sláma *et al.* 2008), and 91500 ($1058.1 \pm 2.8 \text{ Ma}$, Wiedenbeck *et al.* 1995).

For the monazite analyses, the monazite standard MAdel was used (TIMS normalisation data: $^{207}\text{Pb}/^{206}\text{Pb} = 490.7 \text{ Ma}$, $^{206}\text{Pb}/^{238}\text{U} = 514.8 \text{ Ma}$ and $^{207}\text{Pb}/^{235}\text{U} = 510.4 \text{ Ma}$, Payne *et al.* 2008), and accuracy was monitored using the in house monazite standard 94-222/Bruna-NW (ca. 450 Ma, Payne *et al.* 2008) and the recognised standard 44069 ($429.9 \pm 0.4 \text{ Ma}$, Aleinikoff *et al.* 2006).

Data was processed and corrected using the GLITTER (ver 4.4.4) software developed by Macquarie University.

Throughout this study, average ages for the GJ-1 standard were 599 ± 2.4 Ma (2σ , $n=57$, MSWD = 1.15), 602.2 ± 2.1 Ma (MSWD = 1.00), and 614.1 ± 8.8 Ma (MSWD = 0.64) for, $^{207}\text{Pb}/^{235}\text{U}$, and $^{207}\text{Pb}/^{206}\text{Pb}$ ages respectively. Average $^{206}\text{Pb}/^{238}\text{U}$ ages for the other standards were 686.7 ± 8.8 Ma (2σ , $n = 5$, MSWD = 0.35) for BJWP, 332.6 ± 3 Ma (2σ , $n = 9$, MSWD = 0.75) for Plesovice, and 1037 ± 17 Ma (2σ , $n = 6$, MSWD = 1.3) for 91500.

Average ages obtained for the monazite standard MAdel were 490.9 ± 6.5 Ma (2σ , $n=58$, MSWD = 0.48), 519.8 ± 2.2 Ma (MSWD = 0.66), and 514.4 ± 1.8 Ma (MSWD = 0.94) for the $^{207}\text{Pb}/^{206}\text{Pb}$, $^{206}\text{Pb}/^{238}\text{U}$, and $^{207}\text{Pb}/^{235}\text{U}$ ages respectively. Average $^{206}\text{Pb}/^{238}\text{U}$ ages for the 94-222/Bruna-NW and 44069 standards were 456.4 ± 4.7 Ma (2σ , $n=10$, MSWD = 0.99) and 445 ± 27 Ma (2σ , $n=10$, MSWD = 30) respectively.

4. OBSERVATIONS AND RESULTS

4.1 THE WARREN INLIER

4.1.1 - LITHOLOGY

The Warren Inlier is comprised of a coarse grained schistose gneiss (Figure 2, 3a-d), herein referred to as the Warren Gneiss. Quartzofeldspathic and mica rich bands are well developed in most outcrops. The gneissic composition varies between quartzofeldspathic dominated (up to 70%) and mica dominated (up to 80%) in throughout the inlier. These lithological variations were considered too minor to warrant separate mapping units as the mineralogy appeared consistent throughout, thus the Warren Inlier has been mapped as a single lithological unit (Figure 2).

In the reservoir Spillway Type Section (Figure 2), the composition of the inlier rocks are typically 50-60% plagioclase, 10-20% quartz, and 20% biotite, with accessory muscovite replacing sillimanite. Trace rutile, garnet, and pyrite are also observed. Locally, muscovite is

the dominant mica, and comprises up to 50% of the whole rock. Sillimanite retrogressed to muscovite is seen abundantly within some outcrops in the southern areas of the inlier, but is rarer in the northern areas and generally only observed in thin section. In some of the mica dominated areas, coarse tourmaline crystals up to 3 cm long are observed. In some rare cases hematite grains up to 5mm are also observed.

The Warren Inlier is host to at least two generations of igneous intrusives. With the exception of infrequent minor leucosomes, the exposed rocks of the Warren Inlier do not appear migmatized, but are intruded by many veins and dykes of pegmatite.

The earliest intrusive (Figure 3a) is a structurally mature, coarse grained pegmatite composed of approximately 30% quartz, 20% biotite, and 50% coarse grained K-feldspar which preserves strong exsolution features and large amounts of quartz inclusions, with minor biotite and muscovite inclusions. Rare inclusions of fine grained pyrite are also observed in quartz, feldspar, and biotite. In these pegmatites biotite defines a strong foliation which has been folded (Figure 3a). These intrusives generally occur as veins up to 40cm thick.

A second generation of pegmatites is also observed, composed primarily of approximately 40% quartz and 60% K-feldspar, with minor traces of biotite and rare fine grained pyrite. In some of the larger pegmatites, accessory beryl and tourmaline are also observed. These younger pegmatites are observed on scales from several centimetres to several meters in thickness. The thinner pegmatite bands are commonly folded (Figure 3b), however the thicker are typically undeformed. No identifiable fabric is present in these pegmatites. In addition to pegmatitic intrusives, rare occurrences of amphibolites are also observed. These are dominantly composed of variable amounts of biotite, hornblende, and plagioclase. It is possible that these amphibolites represent an igneous mafic protolith, although previous work has suggested a marl protolith for such rocks (Mills 1973). During this study, these amphibolites were only seen in two localities; as prominent layers in the Spillway Type

Section (Figure 4) and a small (~1 m) exposure in the central inlier (coordinates 0309661mE 6154835mN).

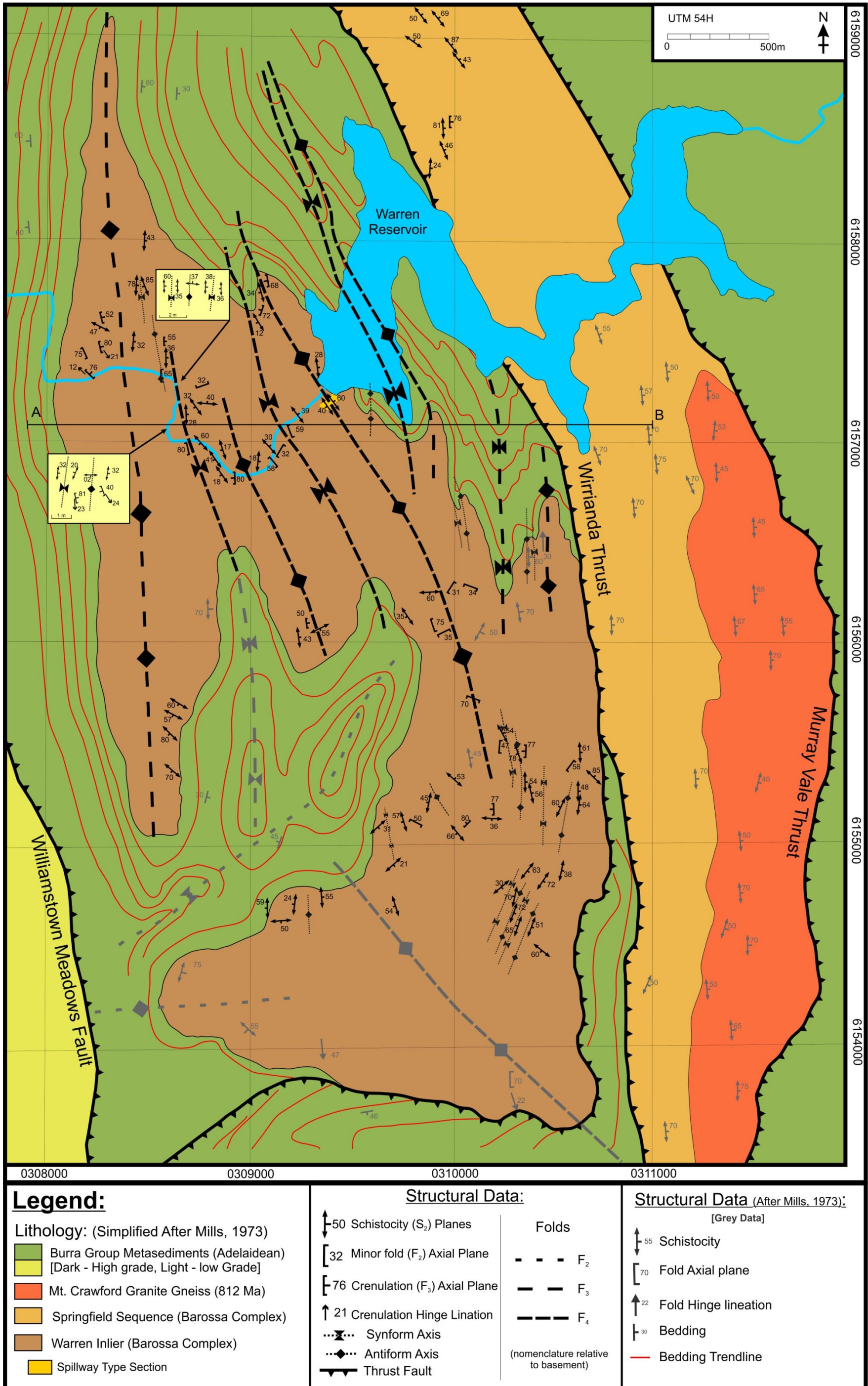


Figure 2: Structural geology map of the Warren Inlier. Note: Grey data represents that presented by Mills (1973)

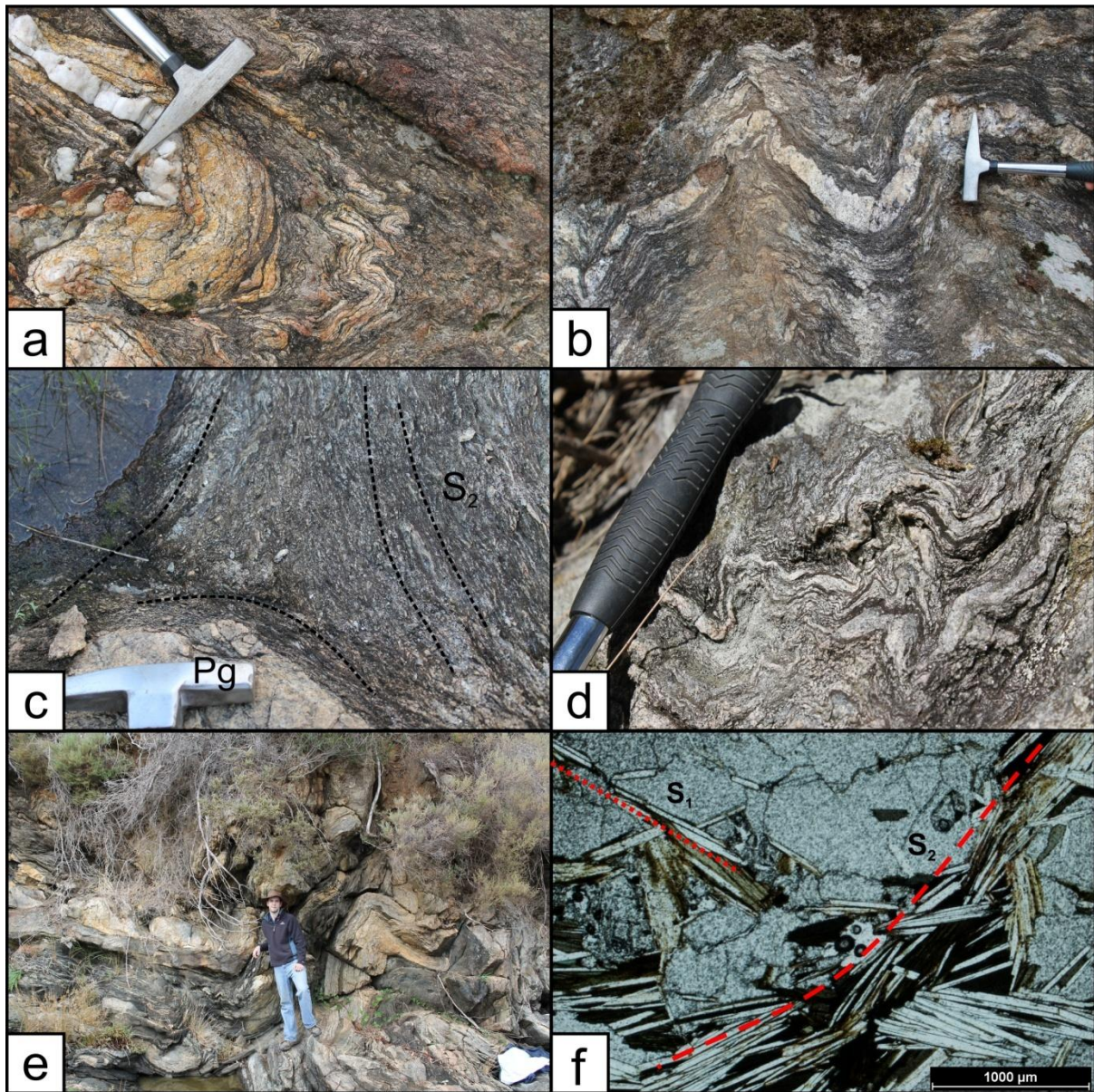


Figure 3: a) Structurally mature pegmatite showing a strong internal fabric which has been subsequently deformed. b) Younger generation of pegmatite which is folded with no internal fabric. c) S_2 schistosity fabric overprinting the early pegmatite. d) Disharmonic folds in Warren Gneiss. e) Outcrop scale folds in the Spillway Type Section. f) Photomicrograph of relict S_1 fabric being overprinted by the dominant S_2 fabric.

4.1.2 - STRUCTURE

The dominant fabric in the Warren Inlier is an S_2 gneissic fabric. A relict S_1 schistosity is visible in thin section, but was not identified in cm thick observed in the field (Figure 3f).

This S_1 fabric is observed as thin layers of mica grains which commonly occur oriented at an angle to the more dominant S_2 fabric (Figure 3f).

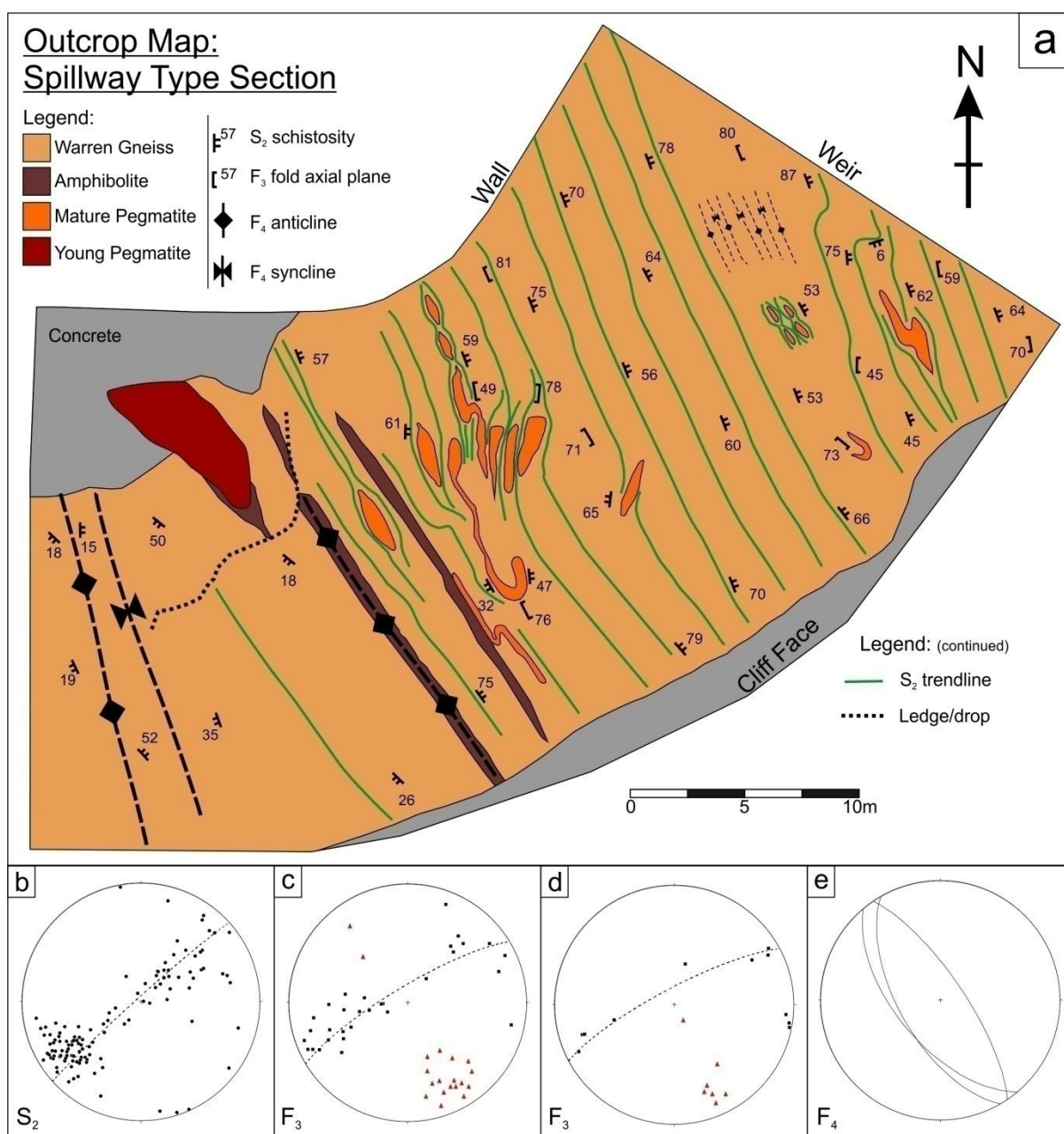


Figure 4: a) Outcrop map of the Spillway Type Section. b) Poles to S_2 fabric showing distribution along a NE-SW profile plane (n=123). c) Poles to F_3 axial planes (black squares, n=35) and F_3 fold hinge lineations (red triangles, n=23). Axial planes show a spread along a NE-SW profile plane. d) Poles to F_3 crenulations (black squares, n=11) and F_3 crenulation hinge lineations (red triangles, n=9). Crenulation axial planes show distribution along a NE-SW profile plane. e) Major F_4 fold axial planes (n=3) which are axial planar to earlier trends. These data demonstrates the coaxial nature of the D_3 and D_4 phases, suggesting that they may represent the same progressive deformation phase.

identifiable from mica layers segregating from the quartz and plagioclase. These bands are typically between 0.5 and 2 mm in thickness. In the southwestern most areas of the inlier the gneissosity is well developed, with quartzofeldspathic and biotite-sillimanite bands up to 2 cm thick observed.

In some outcrops where the early generation pegmatite is present, the S_2 fabric is observed to have formed around the pegmatite, indicating that the S_2 fabric developed synchronous to or post dates this early intrusion (Figure 3c).

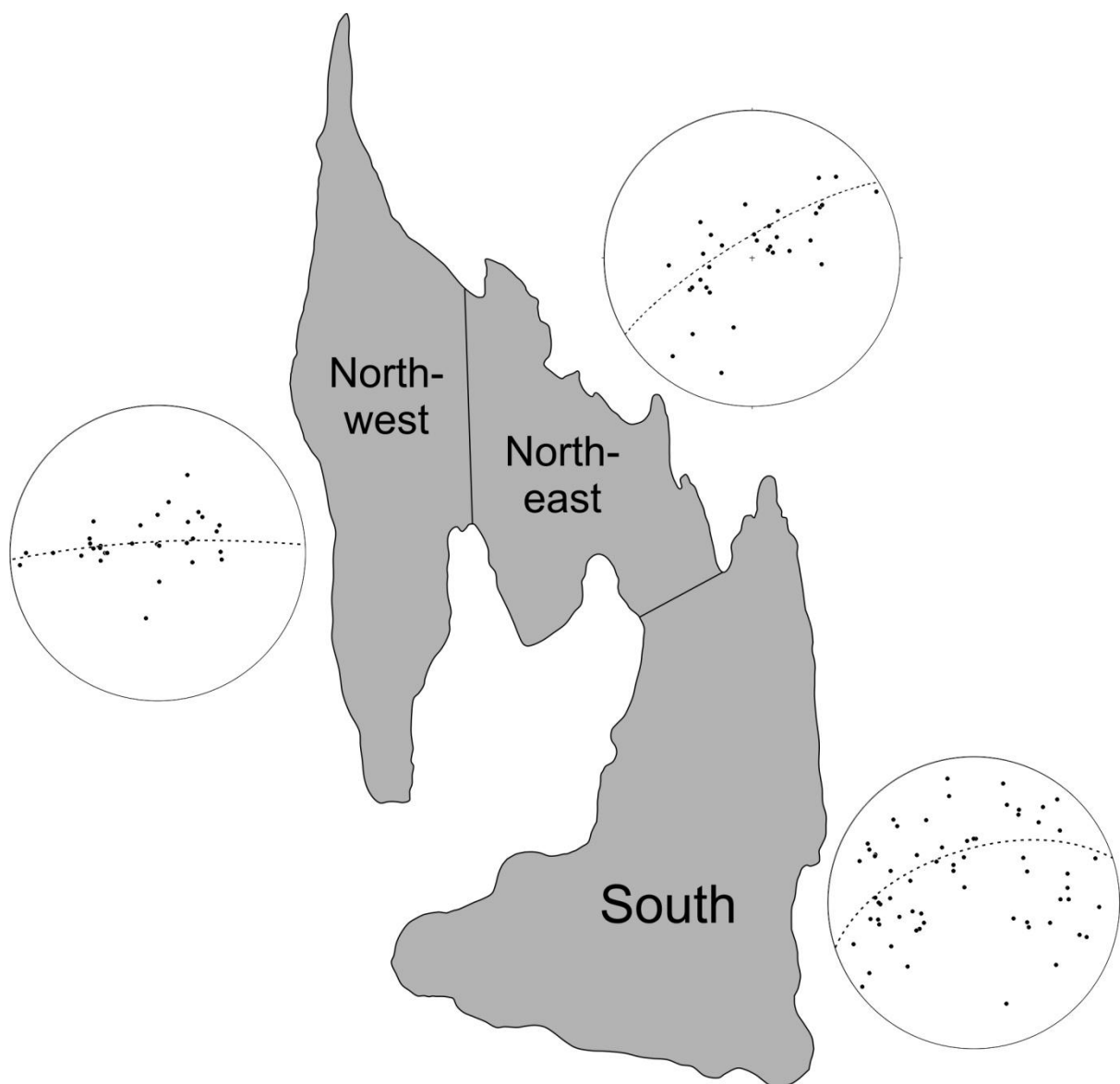


Figure 5: Equal area stereonet plots of poles to S_2 schistosity. The northwest area shows a spread of S_2 poles that spread around an east to West profile plane, indicating north-south trending fold axes (n=32). The northeast area shows a spread of S_2 poles depicting a best fit profile plane striking NE-SW, indicating northwest-southeast trending fold axes (n=33). The Southern area displays less discernable trends when broken into subareas, and is presented as one area. This area shows a weak S_2 spread from ENE-WSW, which is likely a reflection of interference from the two recognised orientations seen in the north (n=65).

The orientation of the S_2 fabric is variable across the inlier due to later folding events (Figure 5). In the north western area of the inlier the schistosity is folded around a north-south trending axis, while in the north eastern area the fold axes trend northwest-southeast (Figure 5). The orientation of the S_2 fabric in the southern inlier is less consistently orientated due to multiple interfering fold events. A weak trend is observable from the south-southwest to north-northeast.

In most outcrops, folds deforming the S_2 fabric of a 3-15 cm scale dominate, which is attributed to an F_3 event. In some outcrops the folded fabric is clearly refolded about a definite axis (Figure 6), indicating an F_4 event. Crenulations of S_2 are common in all outcrops and locally can be seen to post date F_3 folds, indicating they are from a late stage, here also attributed to F_4 . The crenulations typically have near vertical axial planes which dip steeply both east and west. The inconsistency here may be due to either a conjugate pair of crenulations forming, or the crenulations formed mid D_4 and underwent further deformation. A stereonet plot of the poles to F_3 axial planes (Figure 7) shows a spread around an east-northeast to west-southwest profile plane. This spread of data is also seen in the schistosity planes in the northeastern area of the inlier, and is comparable to the weak trend observed in the southern area. As folds of this orientation are deforming the F_3 folds, they are attributed to the F_4 event. This event is clearly seen in the Spillway Type Section where large scale folds are observed deforming the S_2 fabric, F_3 axial planes, and F_4 crenulations (Figure 4b-e). The similar orientation of F_3 and F_4 suggest that D_3 and D_4 are coaxial and may represent fabric formation stages in the same progressional deformation.

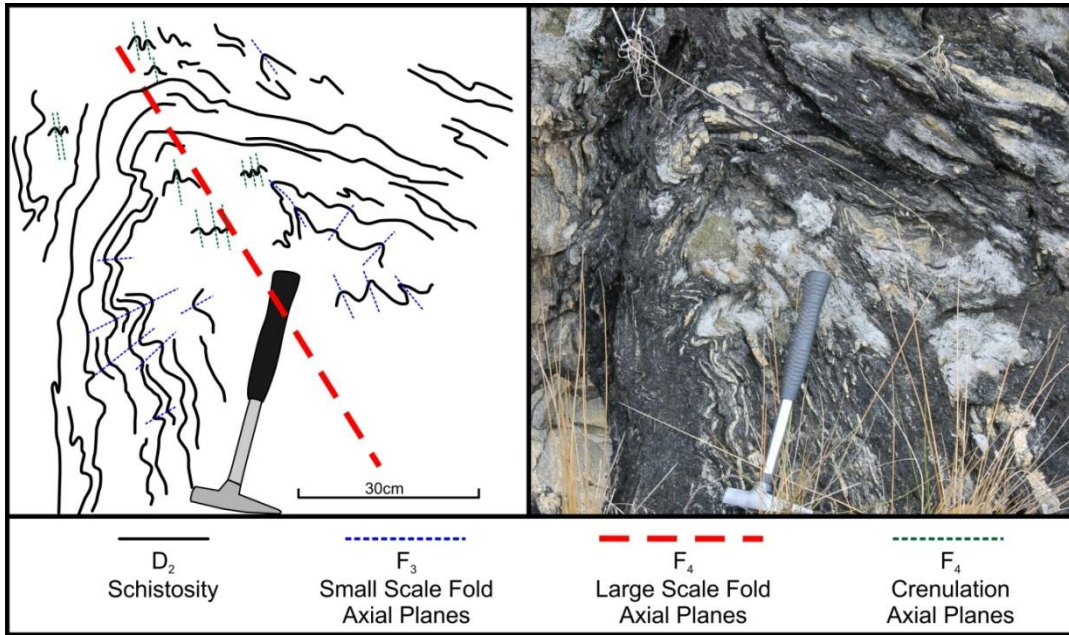
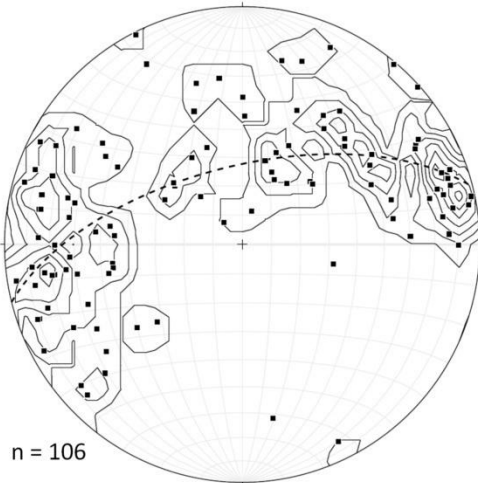
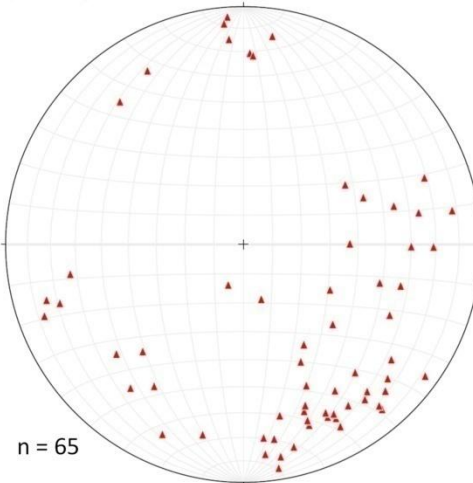


Figure 6
(Left): Sketch of outcrop in Spillway Type Section showing F_3 folds coaxially refolded around the F_4 axis

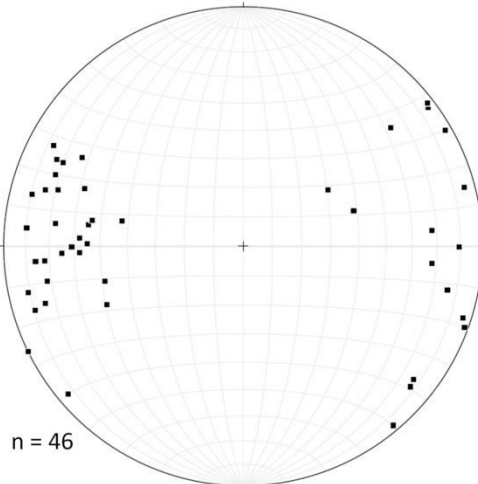
a) F_3 Poles to Axial Planes



b) F_3 Hinge Lineations



c) F_4 cren. Poles to Axial Planes



d) F_4 cren. Hinge Lineations

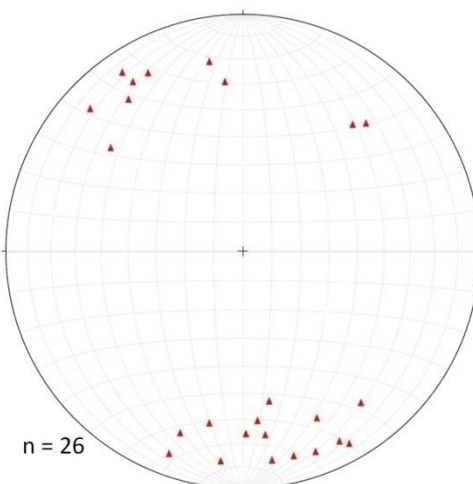


Figure 7 (Left): Fold data collected from the entire Warren Inlier

a) Density contours of poles to F_3 axial planes, showing clusters of upright roughly N-S striking fold axial planes, which show a spread around an ENE-WSW plane. b) F_3 fold hinge lineations which show a SE clustering. c) F_4 poles to crenulation axial planes showing a distinct e-w clusters but with significant spread to the NE, possibly due to D_4 or a later e-w trending fold phase. d) F_4 crenulation hinge lineations showing clustering to the south

4.1.3 - GEOCHRONOLOGY

Three samples of the Warren Gneiss, and two pegmatites of differing structural generation were sampled for LA-ICP-MS U-Pb geochronology from within 100 meters of the Spillway Type Section. In the samples of Warren Gneiss detrital zircons were not identified, however monazite was abundant in the Warren gneiss, as were zircons in the two generations of pegmatites and were used for U-Pb dating.

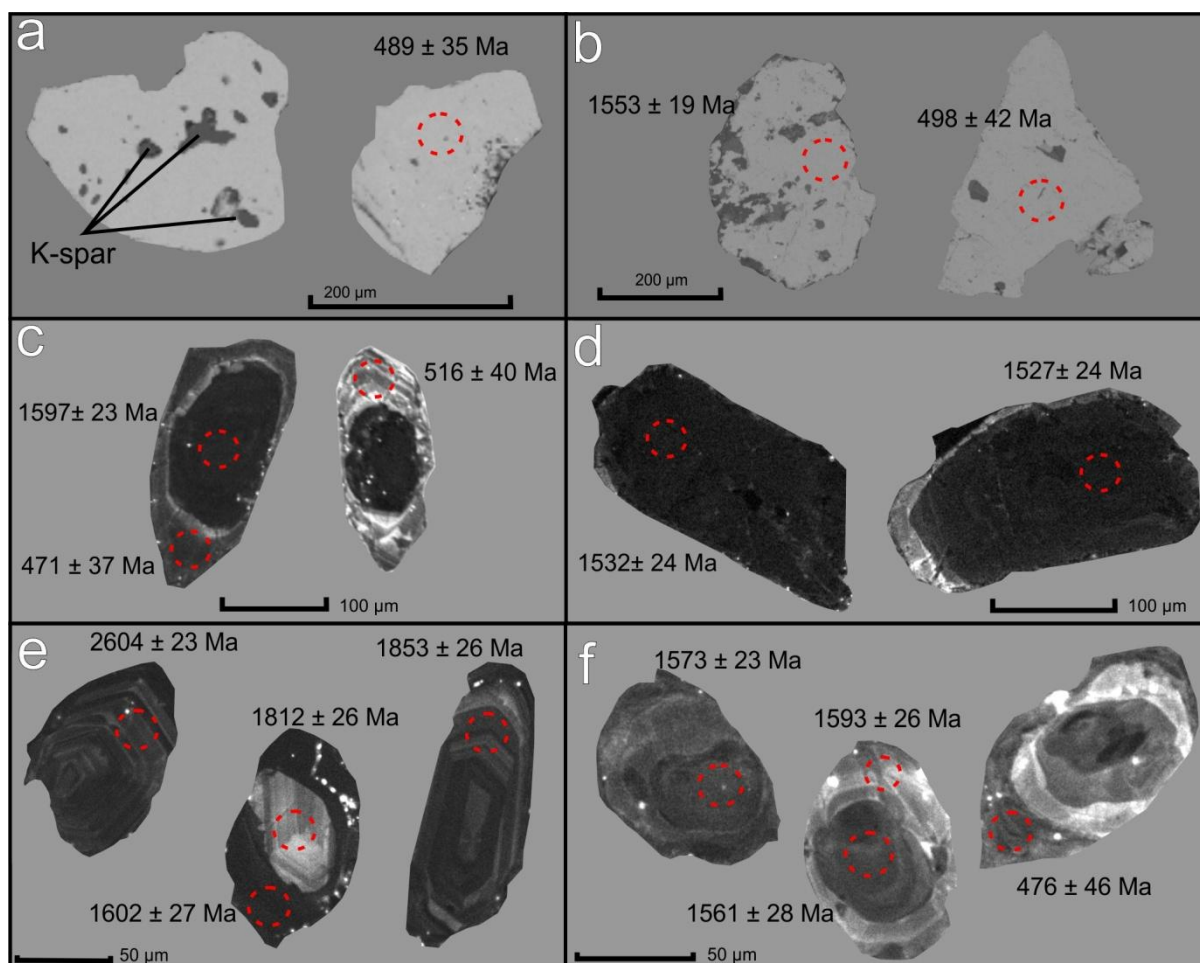


Figure 8: CL and BSE images of analysed zircon and monazite grains. a) BSE images of monazites from sample KM12-05. b) BSE images of monazite grains from sample KM12-08. c) CL images of zircon grains from sample KM12-01 showing inherited cores and oscillatory zoning in magmatic rims. d) CL images of zircon grains from sample KM12-07. Zoning is obscured by dark colouration. e) CL images of detrital zircon grains from sample KM12-17. f) CL images of metamorphic zircons from sample KM12-11

Monazite geochronology:

In both samples of Warren Gneiss monazite grains were typically an opaque honey colour with equant to irregular crystal shapes and sizes ranging from 100 to 400 μm in diameter.

Small inclusions of K-feldspar were observed in many grains (Figure 8). No internal zoning was detected under BSE imaging in any of the grains dated.

Sample: KM12-05

Eighty two analyses were conducted on resin mounted monazite grains. Two age populations are apparent in this sample (Figure 9). The older population is only represented by 4 grains, which show some resetting towards the younger population.

The older population has an average $^{207}\text{Pb}/^{206}\text{Pb}$ isotopic age of 1568 ± 21 Ma ($n=4$, 2σ , $\text{MSWD} = 0.57$). The younger population shows a small spread of ages, which suggests progressive crystallisation throughout the duration of the event. For grains that are within 5%

concordant, a weighted average of $^{207}\text{Pb}/^{206}\text{Pb}$ ages gives 484 ± 9 Ma ($n = 38$, 2σ , $\text{MSWD} = 0.25$).

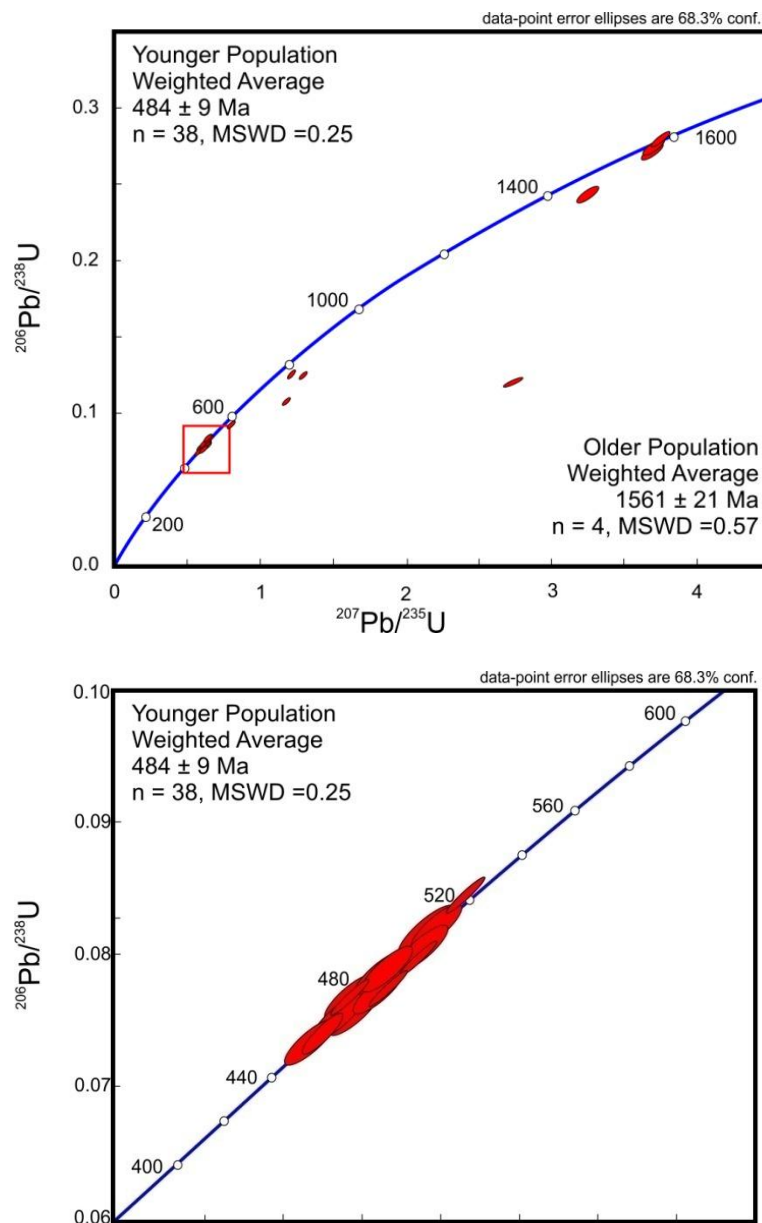


Figure 9: Concordia plots for monazite analyses from KM12-05. Top – all data, bottom – blow up of red square in the top plot, showing the younger population

Sample: KM12-08

Fifty analyses were conducted on resin mounted monazite grains.

Two age populations were evident, with a stronger signal for the older age. For the younger population a weighted average of $^{207}\text{Pb}/^{206}\text{Pb}$ ages gives 502 ± 28 Ma ($n=5$, 2σ , $\text{MSWD} = 0.98$).

Older grains were less concordant, with a large number displaying reverse discordancy (Figure 10). Using data that is within 95% concordancy, a weighted average of $^{207}\text{Pb}/^{206}\text{Pb}$ isotopic ages gives 1506 ± 16 Ma ($n = 18$, 2σ , $\text{MSWD} = 2.4$).

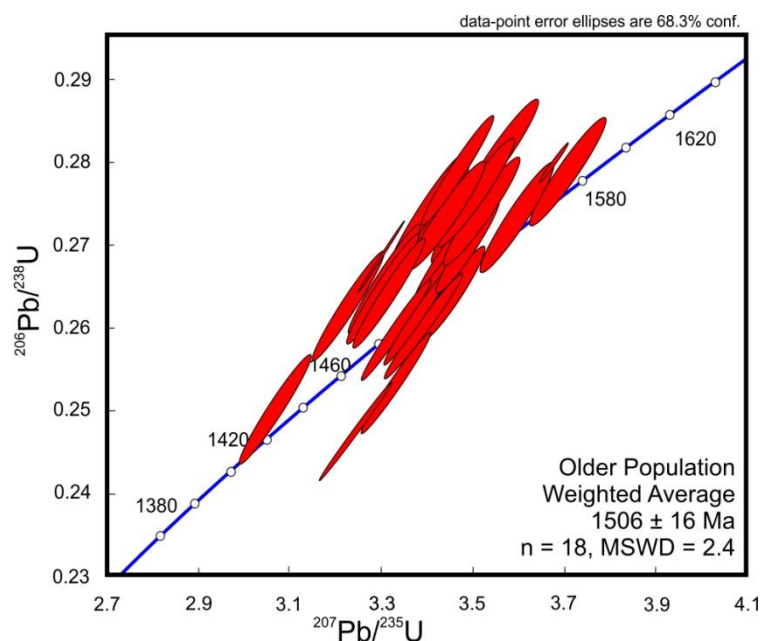
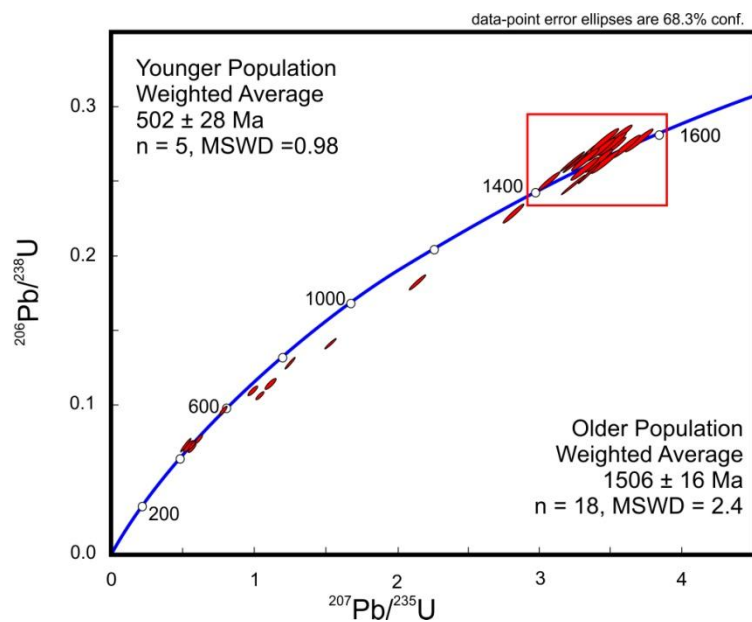


Figure 10: Concordia plots of monazite analyses from KM12-08. Top – All data. Bottom – Blow up of the red square in the top figure, showing the older population

Zircon Geochronology:Sample: KM12-01

Twenty five analyses were conducted on twenty four resin mounted zircon grains, which were separated from a structurally immature pegmatite collected from the Adelaidean cover sequence 70 meters past the unconformity boundary with the inlier. Zircon grains were typically

elongate and euhedral, however some grains were more anhedral and equant in shape.

Under CL imaging grains were typically dark and homogeneous, with few grains displaying magmatic growth rims. Magmatic rims, where present, were typically brighter and displayed oscillatory zoning (Figure 8).

Two age populations were observed in this sample, corresponding to cores and magmatic rims (Figure 11).

The cores showed some Pb loss along a discordia towards the younger age, and, for analyses that were within 10% concordancy, had an average $^{207}\text{Pb}/^{206}\text{Pb}$ isotopic age of 1570 ± 13 Ma ($n=15$, 2σ , MSWD = 0.31). The magmatic rims had an average $^{207}\text{Pb}/^{206}\text{Pb}$ isotopic age of 518 ± 37 Ma ($n=4$, 2σ , MSWD 1.12).

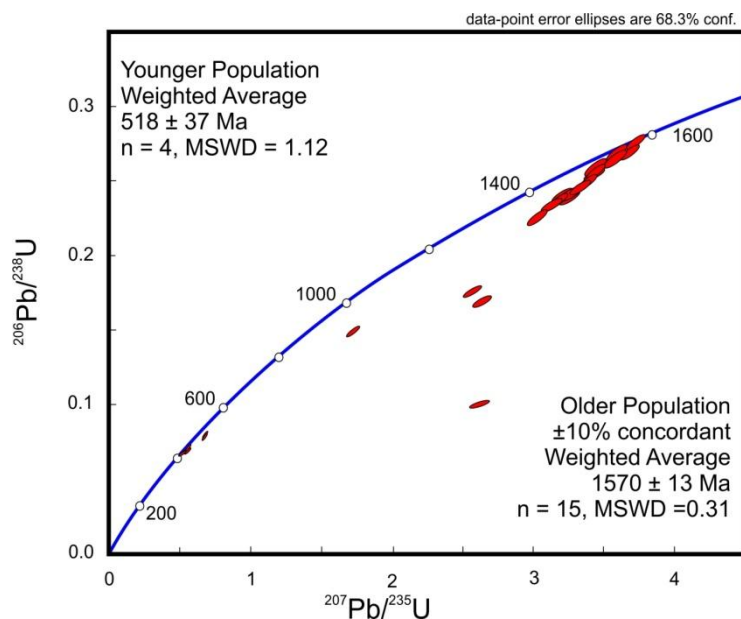


Figure 11: Concordia plot of zircon analyses from sample KM12-01

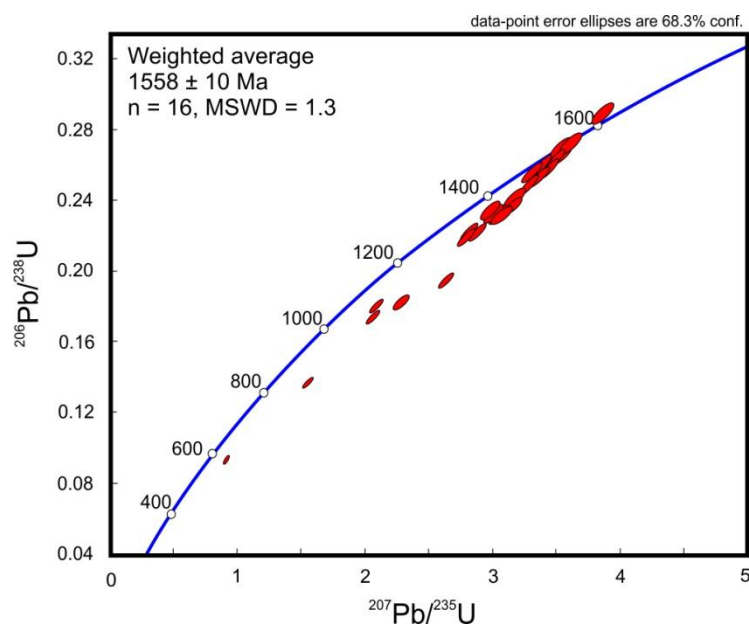


Figure 12: Concordia plot of zircon analyses from sample KM12-07

Sample: KM12-07

Twenty nine analyses were conducted on 24 resin mounted zircon crystal, which were separated from a structurally mature pegmatite intrusion from within the basement. Zircon grains were typically subhedral to anhedral, with typically elongate grain shapes. Many grains were cracked or metamict due to radiation damage. Under CL imaging most grains appeared dark and homogeneous, with no obvious zones of different age growths. Oscillatory zoning was evident in few grains, often obscured by the dark colour of the grains under CL imaging. For analyses that were within 10% concordancy, an average $^{207}\text{Pb}/^{206}\text{Pb}$ isotopic age gives 1558 ± 10 Ma ($n=16$, 2σ , MSWD 1.3) (Figure 12).

4.2 - THE SPRINGFIELD SEQUENCE

The area of focus in the Springfield Sequence was a small area north of the Warren Reservoir and immediately east of the Williamstown kaolinite-sillimanite deposit. Detailed lithology is presented by Ringenbergs (1975) and built upon by Conor (1984), so only a brief summary of field observations is presented.

4.2.1 - LITHOLOGY

Two units were observed in the focus locality, which were consistent with the Sillimanite Quartz Gneiss and the Mica Schist as described by Ringenbergs (1975). In both rock types sillimanite is observed in all samples, in many cases being pseudomorphed by muscovite or sericite. For some areas within the schist, large laths of kyanite (up to 10 cm) are seen in outcrop, however in thin section these are observed to be partially or completely pseudomorphed to fibrolitic sillimanite and muscovite. Quartz, plagioclase, biotite, and

chlorite are commonly seen in varying amounts, but not in all samples. Rutile is a common accessory and is often observable in hand specimen.

4.2.2 – STRUCTURE

A schistosity was the dominant fabric in this area, which dipped relatively consistently towards east-northeast. The generation of the dominant schistosity measured (i.e. S_1/S_2) was

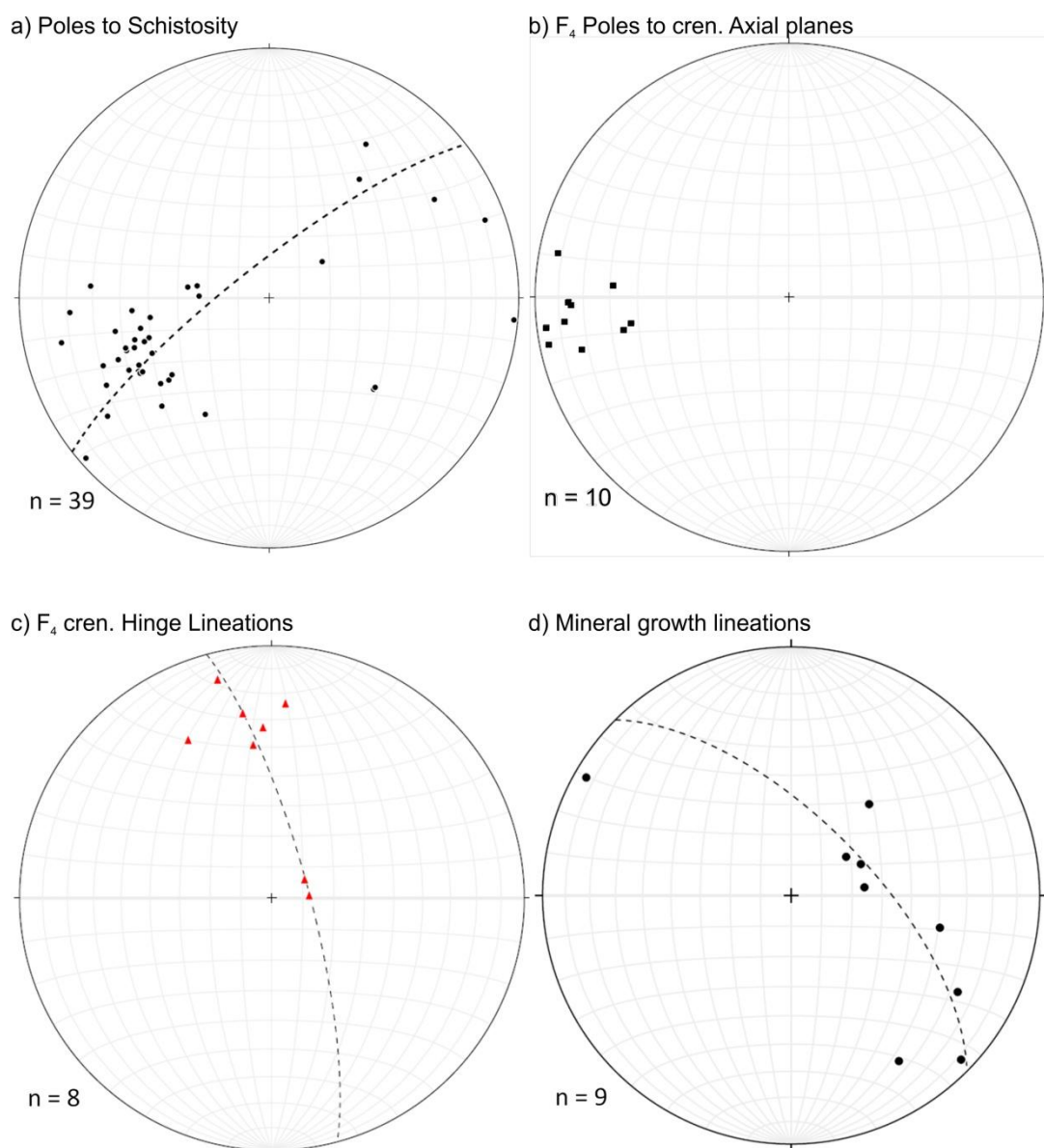


Figure 13: Equal area stereonet projections of measurements from the Springfield Shear Zone. a) Poles to schistosity planes showing minor spreading along a NE-SW trending axis. b) Poles to crenulation axial planes, showing clustering to the west. c) Crenulation hinge lineations, showing minor spreading along a NNW-SSE trending axis. d) Mineral streaking lineations showing minor spreading along a NW-SE trending axis

not specifically identified in this study, however both Mills (1973) and Ringenbergs (1975) described the dominant schistosity as an S_2 , and is here considered as such. Some minor folds, up to several meters in wavelength, create a spread in the schistosity measurements from Southwest to Northeast when plotted on a stereonet (Figure 13a). Crenulation axial planes were seen to dip consistently to the east (Figure 13b) but were not aligned with the axis described by the schistosity trendline, indicating that they formed at a later stage.

The hinge lineations of these crenulations showed a weak spread along a north-south striking trendline (Figure 13c), and a similar trend was observed in mineral growth lineations (Figure 13d), and it could also be argued that the schistosity is also being spread around this axis. This is consistent with the late stage folds described in the Warren Inlier.

4.2.3 – GEOCHRONOLOGY

Sample: KM12-11

KM12-11 is from a tourmaline bearing sillimanite-mica-chlorite schist. Zircon grains typically ranged from 50 to 100 μ m in size, were anhedral in shape, and were typically colourless and transparent. Oscillatory zoning was typically not observed, however thicker homogeneous bands interpreted as metamorphic growth zoning occurred in many grains (Figure 8f).

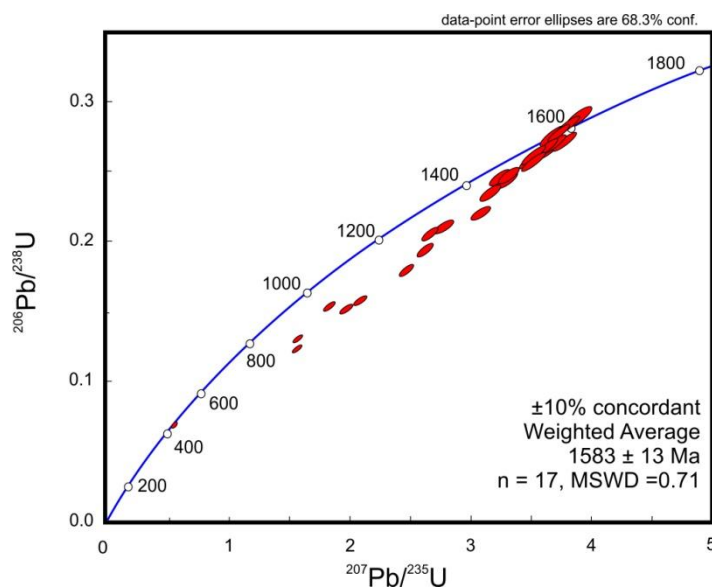


Figure 14: Concordia plot of zircon analyses from sample KM12-11

Of more than a hundred mounted grains, only 30 were large enough or had zones large enough to perform a reliable analysis, in which both cores and rims were analysed. Only one dominant age population was observed, with a single younger grain present recording ca. 476 Ma. Many analyses showed lead loss, and concordancy ranged from 54% to 104%. An average $^{207}\text{Pb}/^{206}\text{Pb}$ isotopic age was calculated from analyses that were within 10% concordancy, which gave 1583 ± 13 Ma ($n=17$, 2σ , $\text{MSWD} = 0.71$) (figure 14).

Sample: KM12-17

KM12-17 is a quartzofeldspathic dominated layer within the Springfield shist. Zircon grains were typically 50 to 100 μm in size, anhedral and rounded, and transparent and colourless in colour. Many grains show inherited cores with sections of overgrowth. The cores commonly preserved oscillatory zoning, with homogeneous metamorphic rims. The shape of the cores were typically rounded, suggesting a detrital origin. Of almost 49 grains mounted, only 27 contained zones large enough to acquire a reliable analysis. Resulting

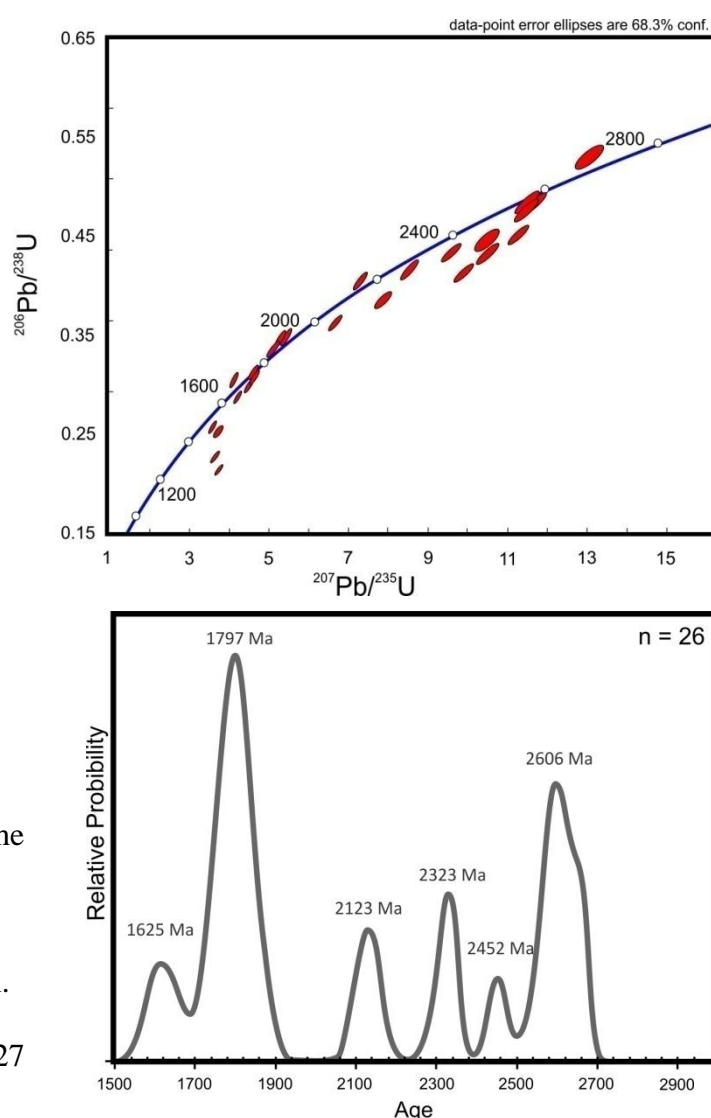


Figure 15: Top - Concordia plot of zircon analyses from sample KM12-17, and, Bottom - probability density diagram of detrital zircon ages

$^{207}\text{Pb}/^{206}\text{Pb}$ ages ranged from 2650 to 1600, with two major age peaks at approximately 2600

Ma and 1800 Ma (figure 15). Minor peaks occur at approximately 2300 Ma, 2100 Ma, and 1600 Ma. Average $^{207}\text{Pb}/^{206}\text{Pb}$ isotopic ages from these peaks give ages of 2606 ± 27 Ma ($n=8$, 2σ , $\text{MSWD} = 1.7$) and 1797 ± 29 Ma ($n=8$, 2σ , $\text{MSWD} = 1.6$). It should be noted that the analyses composing this ~ 1800 Ma peak contain ages ranging from 1744 to 1853 Ma and likely represents multiple sources.

Two smaller peaks, each containing only 2 points each, give average $^{207}\text{Pb}/^{206}\text{Pb}$ isotopic ages of 1623 ± 23 Ma ($n=2$, 2σ , $\text{MSWD} = 1.3$) and 2323 ± 35 Ma ($n=2$, 2σ , $\text{MSWD} = 0.11$).

4.2.4 - Th/U Ratios

Sample: KM12-11

A comparison of Th/U ratios against $^{207}\text{Pb}/^{206}\text{Pb}$ isotopic ages (Figure 16) show a cluster of low (>0.1) Th/U ratios for ~ 1580 Ma grains. In the same age bracket, a second smaller cluster occurs around a 0.15 ratio. A small number of outliers describe a spread up to a 1.1 ratio. The single young grain in this sample (~ 480 Ma) presents a Th/U ratio of 0.11.

As the majority of these values

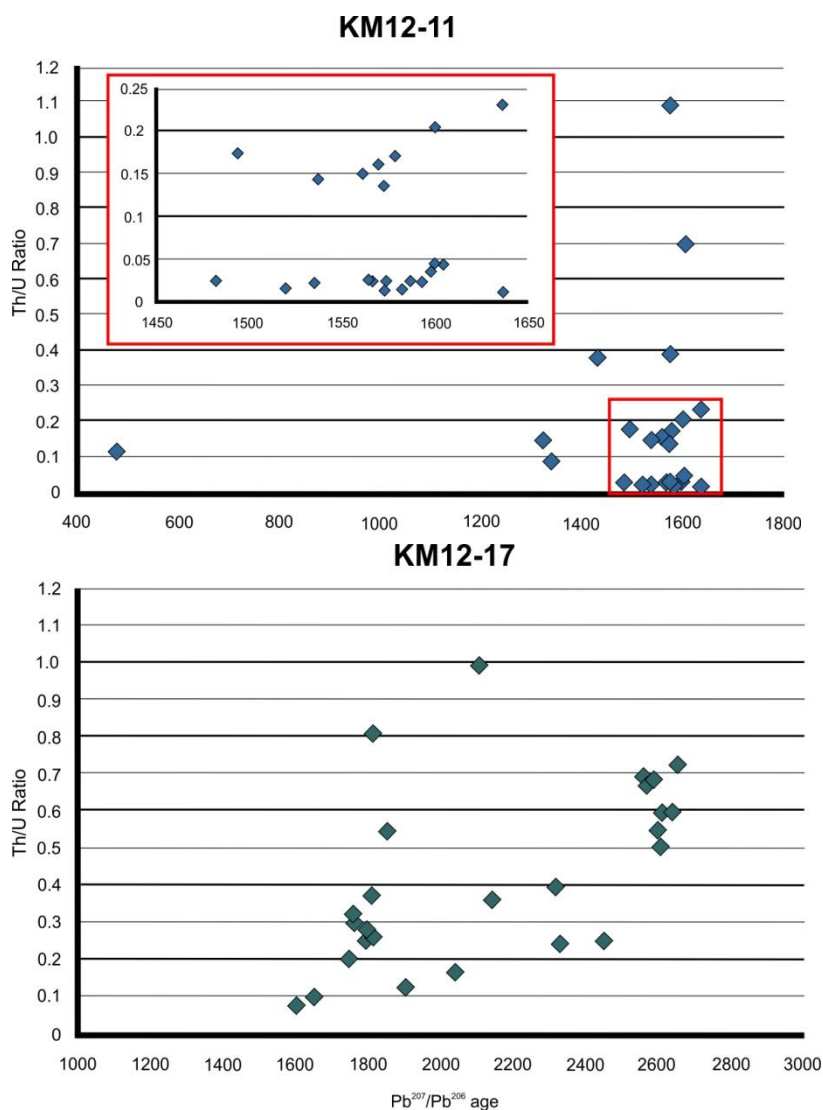


Figure 16: Th/U ratio vs. $\text{Pb}^{207}/\text{Pb}^{206}$ ages plots for samples KM12-11 (top) and KM12-17 (bottom)

are less than .2, this, combined with the relatively uniform age distribution at ~1580 Ma, indicates that this population is of metamorphic origin and is not a detrital population.

Sample: KM12-17

A plot of Th/U ratios against $^{207}\text{Pb}/^{206}\text{Pb}$ isotopic ages (Figure 16) shows a distinct cluster corresponding to the ~2600 Ma detrital peak at a ratio value of 0.5 – 0.7. The ~1800 Ma peak also corresponds to a cluster between ratio values of 0.2 – 0.4, with minor outliers spreading up to ratios of 0.8. These ratios suggest a magmatic source for these two zircon populations. The two points corresponding to the ~1625 Ma age plot at approximately 0.1, indicating a metamorphic origin.

5. DISCUSSION

5.1 INTERPRETATION OF GEOCHRONOLOGICAL DATA

The two Mesoproterozoic monazite ages obtained in this study, 1568 ± 21 Ma and 1506 ± 16 Ma, do not overlap within error. However, the number of reversely discordant analyses and high MSWD (2.4) for the younger of these ages (sample KM12-08) suggest that this age may not be reliable. As the 1568 ± 21 Ma age has better statistics, and overlaps within error of a published monazite age for the Barossa Complex (1579 ± 7 Ma, Szpunar *et al.* 2007) this age is considered reliable.

The metamorphic zircon age from the Springfield Sequence at 1583 ± 13 Ma also indicates a high grade event at this time. However, the age from the mature pegmatites is notably younger at 1558 ± 10 Ma. While this overlaps within error of the reliable monazite age from the Warren Gneiss, it does not overlap with the published ages or the metamorphic zircons from the Springfield Sequence.

Rutherford *et al.* (2007) presented monazite ages from the Curnamona Province relating to the Olarian Orogeny from 1610 Ma to 1585 Ma, as well as a retrograde metamorphic event from 1570 Ma to 1550 Ma. No magmatism has been reported associated with the latter event in the Curnamona province, and no magmatism is reported of this age in this part of the Gawler Craton. Thus, it is unclear whether the age of this pegmatite represents a separate event to the ~1580 Ma event at ~1560 Ma, as in the Curnamona Province, or whether there is a minor discordancy of the pegmatite age. If this does represent a retrograde event, it could be argued that the 1568 ± 21 Ma age reflects this, rather than an event closer to 1580 Ma.

Monazite U-Pb geochronology from the Warren Gneiss give ages of 502 ± 28 Ma and 484 ± 9 Ma, which coincide with established ages for the Delamerian Orogeny (Foden *et al.* 2006).

The large error margins on these ages make it difficult to pinpoint a precise age of metamorphism, however the spread of analyses on the concordia plots over ~40 m.y. suggest that the crystallisation of monazite at this time occurred progressively throughout the event.

It is also notable that the ages from the inherited cores in the young pegmatite presented only a single age of 1570 ± 13 Ma, suggesting it was likely sourced from a detrital poor part of the Barossa Complex which experienced metamorphic zircon growth, such as that seen in KM12-11.

The metamorphic zircons from the Springfield Sequence at 1583 ± 13 Ma confirm that this area cannot be an Adelaidean metasediment. This is also supported by the detrital zircon populations. If this were to be an Adelaidean metasediment, detrital zircon ages would be expected to include peaks at 1560, 1300, 1100, 1050, and 980 Ma, as has been reported for the Burra Group (Ireland *et al.* 1998), which are not observed.

The detrital zircons from the Springfield Sequence show significant peaks at 2600 Ma and 1800 Ma. No ages occur younger than 1602 ± 27 Ma. Th/U ratios from the 2 ~1625 Ma

analyses suggest that they are of metamorphic origin, and as they are from homogeneous growth rims (Figure 8e) and correspond with a documented metamorphic event in the Barossa Complex (1625 ± 9 Ma, Belousova *et al.* 2006), these are interpreted to have grown post deposition. The youngest detrital zircon is therefore considered to be 1744 Ma. Some of these detrital ages have possible source regions from elsewhere in the Gawler Craton. Of the concordant grains, three show ages between 1760 and 1744 Ma which correspond to the volcanics associated with the Wallaroo Group (Fanning *et al.* 1988). Two grains record ages of approximately 1792 Ma, which corresponds to the Myola volcanic, located west of the Wallaroo Group (Fanning *et al.* 1988). Two single grains recording 2450 Ma and 1853 Ma suggest input from the Sleaford Complex (Swain *et al.* 2005) and the Donington Suite (Parker *et al.* 1993) respectively.

Three grains which present an age of ~ 1810 Ma are more enigmatic, as no source of this age has been identified in the Gawler Craton (Hand *et al.* 2007), as is the case for the seven grains presenting ages of between ~ 2600 to 2650 Ma. The metasediments of the Sleaford Complex contain a significant input of ca. 2600 Ma detrital zircons, however the source of this input is still yet to be identified (Swain *et al.* 2005). It is possible that the Sleaford Complex is the source of these grains, however, without a more substantial input of Sleafordian Orogeny aged grains, it is more likely that these grains represent input from an external source.

5.2 STRUCTURAL EVOLUTION OF THE WARREN INLIER AND SPRINGFIELD SEQUENCE

The S_1 fabric of the Warren Inlier preserves a metamorphic event which occurred prior to the formation of the S_2 at ~ 1560 Ma. Due to the nature of the S_1 fabric, which is only observed as a relict fabric in thin section samples, the nature and timing of the event responsible for its formation remains enigmatic.

The Warren Inlier is dominated by an S_2 schistosity which has been multiply deformed by the ca. 514 – 490 Ma Delamerian orogeny. Pre-Delamerian folds are only observed in the 1558 ± 10 Ma pegmatites which are observed to structurally pre-date the S_2 fabric. All folds deforming the S_2 are consistent with folds observed in the overlying Adelaidean sequences (Mills 1973). The F_3 and F_4 folds mapped in the basement, synchronous to the Delamerian F_2 and F_3 , evolved coevally in a progressive deformation with an east-west to northeast-southwest principle stress orientation. A spread of S_2 schistosity in the southern inlier (figure 5) suggests a later stage event with a northwest-southeast orientation, however structures of these orientations were not directly observed in this study. The orientation of these late stage structures are consistent with folds in the Burra Group described by Mills (1963, 1973) as F_1 . These folds appear to disturb the axial traces of the F_3 and F_4 folds of the basement (Figure 2), as well as create a late stage spread of the southern S_2 planes around this axis (Figure 5), indicating that they are of a later stage. These folds were poorly described in these earlier studies, and it is possible that they were misinterpreted.

The upright, open, and symmetrical nature of these folds suggest that the S_2 fabric was approximately horizontal when it was deformed. A layer parallel schistosity was described by Mills (1973) in the Burra Group, as has been described elsewhere in the high grade zone of the Delamerian Orogen (Mancktelow 1990, Oliver & Zakowski 1995, Sandiford *et al.* 1995), which along with the strong Delamerian monazite ages, the argument could be made that the S_2 fabric of the Warren Gneiss is of early Delamerian origin.

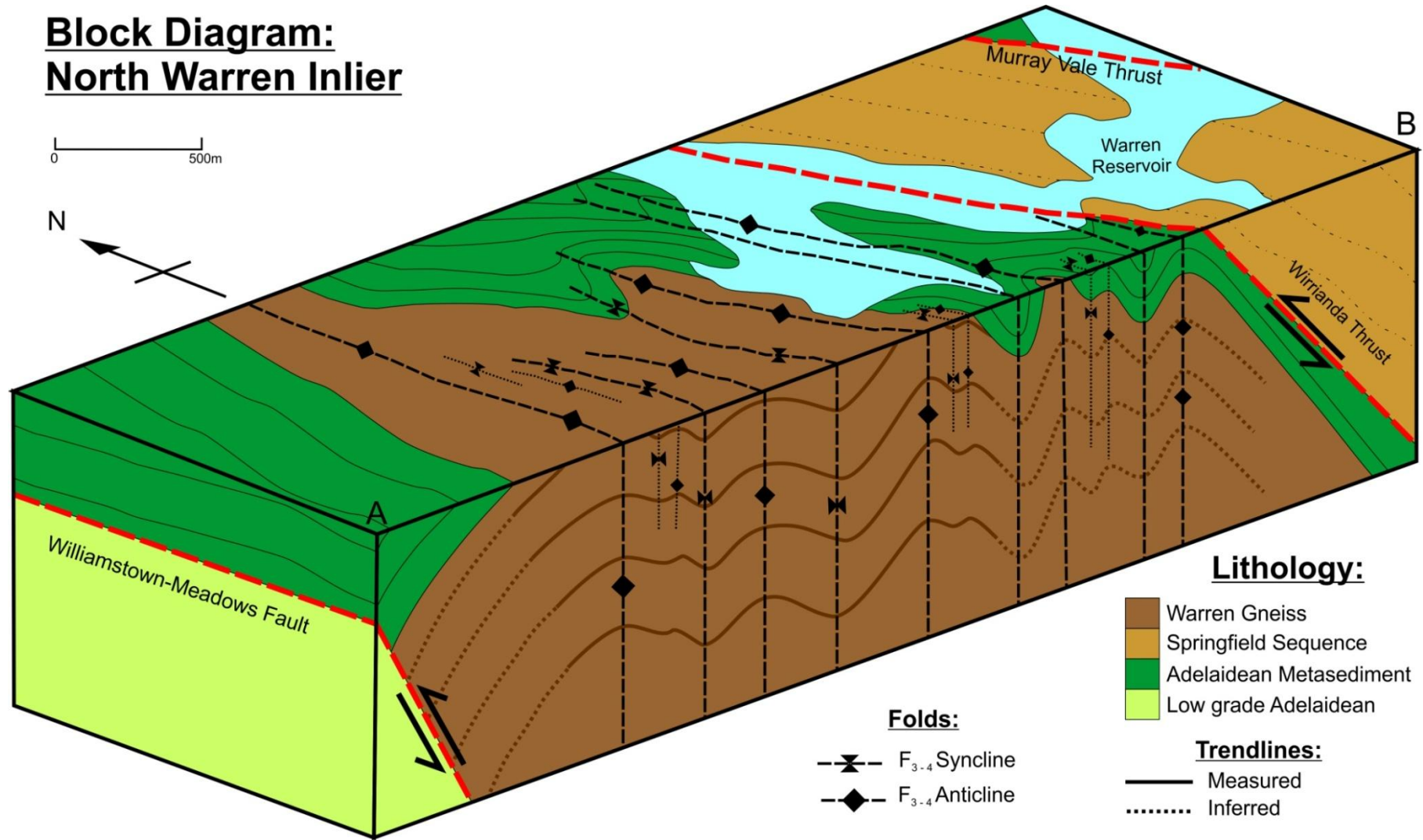


Figure 17: Block diagram of the northern Warren Inlier showing open, upright, symmetrical regional fold orientations, which continue into the Burra Group cover sequence. Cross section line A-B as marked on Figure 2.

However, Mills (1973) described an angular unconformity between the Warren Gneiss and the Burra group. Descriptions and field sketches (Figure 18) of this indicate that the layer parallel S_1 of the Burra Group and the S_2 of the Warren Gneiss, although similar in orientation, are still at an angle to one another. This demonstrates that the S_2 of the Warren Gneiss predates the deposition of the Burra Group and thus represents a Proterozoic fabric. The S_2 fabric is seen to structurally post date the 1558 ± 10 Ma pegmatites and is therefore most likely to be of 1621 ± 21 Ma age.

The implication of this is that the Delamerian monazite ages more likely represent a recrystallisation or resetting age rather than a primary crystallisation age.

Contrasting the Warren Inlier, the S_2 fabric in the Springfield Sequence is unlikely to be ~1560 Ma in age, as this fabric was documented by

Mills (1963, 1973) to continue through the Mt.

Crawford granite gneiss, which has been dated at

812 ± 6 Ma by Preiss *et al.* (2008). The fabric of the

Springfield Sequence dips relatively consistently 50

– 70° to the east-northeast and shows less

deformation by folding at smaller scales than the

Warren Inlier. Where present, large scale folds are

asymmetric with shorter western limbs, which

suggests that this fabric was not near horizontal

during deformation as is the case in the Warren

Inlier. The F_3 folds and F_4 crenulations are

consistent with the deformation in the Warren Inlier, with a likewise potential for a late stage

east-west oriented late stage folding event.

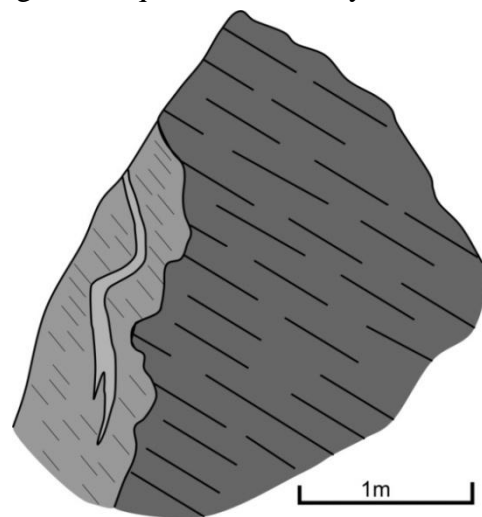


Figure 18: field sketch of angular unconformity from Mills (1973, Figure 3f). From left: Burra group displaying Delamerian S_1 schistosity, bedding described by heavy mineral laminations (light grey), and irregular contact horizon with the Warren Gneiss (dark grey) displaying S_2 fabric. Note angle between Burra group S_1 and Warren Gneiss S_2 .

From this it is interpreted that the dominant schistosity of the Springfield Sequence formed during the Delamerian Orogeny, potentially consequent to the thrusting which emplaced this allochthonous sheet into the cover sequence.

5.3 Implications of this study

A significant metamorphic event is recorded in the Springfield Sequence at approximately 1580 Ma. This corresponds to a metamorphic event previously recorded in the Myponga Inlier (Szpunar *et al.* 2007). This has been linked to a wide scale metamorphic event which affects the Barossa complex, the eastern and central-north Gawler Craton in the Mt. Woods Inlier (Forbes *et al.* 2011, Forbes *et al.* 2012) and the Coober Peedy Ridge and Mabel Creek regions (Cutts *et al.* 2011), to the Chewings orogeny in the Arunta Inlier in Central Australia (Collins & Shaw 1995), and to the Olarian Orogeny in the Curnamona Province (Raetz *et al.* 2002, Forbes *et al.* 2008). This timing also coincides with magmatism in the Gawler Craton which produced the Gawler Range Volcanics and the Hiltaba Granite suite from 1590 to 1575 Ma (Creaser & Cooper 1993, Flint *et al.* 1993), which is attributed to mantle plume related hotspot magmatism (Betts *et al.* 2007, Betts *et al.* 2009).

The rocks of the Warren Inlier record an igneous event at ~1560 Ma, and a metamorphic event at this time which formed the S₂ fabric, in addition to that recorded at ~1580 Ma. If this is the case, then the Barossa Complex record the same metamorphic history as that seen in the southern Curnamona Province (Rutherford *et al.* 2007).

The detrital spectrum from the lower Willyama Supergroup (Page *et al.* 2005, Barovich & Hand 2008) (Figure 19) shows similarity to that of the Springfield Sequence, with a major inputs of 1780, 1820, and 1850 Ma, as well as minor contributions at ~2300, and 2600-2700 Ma. The similarity between these detrital spectra indicate that the Springfield Sequence and

lower Willyama Supergroup were likely linked by source regions. There is also a ~1700 Ma peak in the Lower Willyama spectrum, which could indicate that if the Barovich & Hand (2008) discussed potential source regions for the Willyama supergroup using REE trace

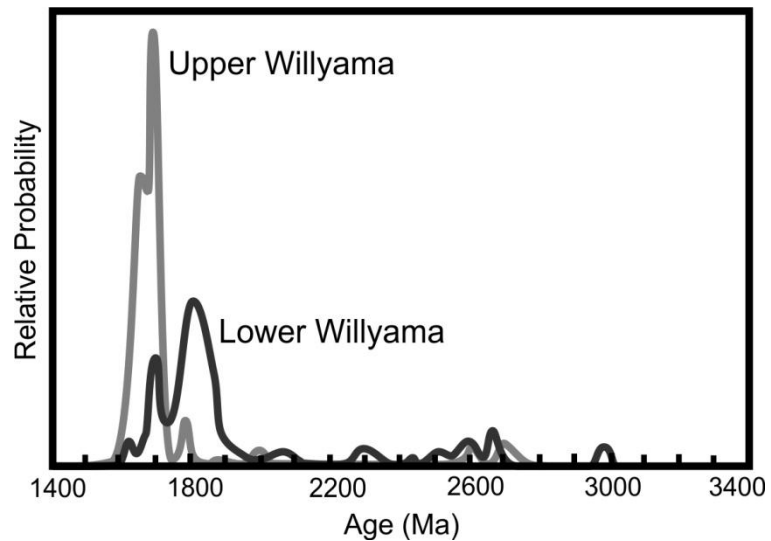


Figure 19: Detrital spectra for the Willyama Supergroup after Barovich & Hand (2008). The Lower Willyama Supergroup (dark line) displays peaks at ~1700 and 1800 Ma, with minor peaks at ~2300 and 2600 Ma

element comparisons and concluded that the Arunta Region as well as the Gawler Craton are likely source areas.

The youngest detrital zircon shows that the protolith of the Springfield Sequence was deposited at a time after 1744 Ma, and an upper limit is provided by the ~1625 Ma metamorphic rims on some of these zircons. The igneous event in the Houghton Inlier at 1718 ± 8 Ma (Belousova *et al.* 2006) provides some constraint for deposition for that inlier.

However, despite temporally coinciding with the Kimban Orogeny, this intrusion could not be classified as either syn-sedimentary or syn-orogenic, and thus cannot be reliably considered a minimum age constraint for the Springfield Sequence. As the rocks of the Houghton Inlier may not represent the same sequence as those of the Springfield Sequence, and this magmatic age is not observed in any of the samples analysed, the minimum depositional age constraint is considered here to be 1625 Ma.

This depositional window follows the evolution of an eastward progression of volcano-sedimentary basins in the eastern Gawler Craton. The earliest is dated by the bimodal Myola

volcanics, which erupted at approximately 1792 Ma (Fanning *et al.* 1988). This is followed by the Wallaroo Group which contains numerous bimodal subaerial and submarine volcanic beds that constrain its depositional age to between 1772 and 1740 Ma (Fanning *et al.* 2007). Owing to the nature of these volcanic, these basins have been attributed to a rift setting (Hand *et al.* 2007). The models presented by Betts and Giles (2006) and Forbes *et al.* (2008) suggest that this rifting was the result of back arc spreading from a subduction zone on the south-western margin (present day coordinates) of the Gawler Craton, and the resulting back arc basin was proposed as the depositional setting of the ~1720 – 1640 Ma Willyama Supergroup in the Curnamona Province (Page *et al.* 2005).

The depositional timing of the Barossa Complex can be constrained to between 1744 and 1625 Ma, which temporally post dates the deposition of the Wallaroo Group and the upper limit pre-dates the onset of deposition of the Willyama Supergroup. From the available constraints it is possible to speculate that the Barossa Complex may represent the easternmost exposure of the Willyama Supergroup.

If the reported magmatic age from the Houghton Inlier represents a synorogenic intrusion at 1718 Ma, a possibility raised by Belousova *et al.* (2006), then this could potentially be considered a minimum age constraint on the deposition of the Barossa Complex. In this instance, an eastward stepping series of basins becomes apparent. The eastward stepping nature of these basins would suggest a migrating depocentre, such as outwards from a continental margin. The volcanic nature of these sediments indicates that this would be an active rather than a passive margin. The most likely tectonic setting if this is the case would be a retreating subduction zone. To further test any relationships between any these regions, it is recommended that a further provenance tool is applied to the detrital zircons of the Barossa complex, such as Hf isotopic or trace element analysis, which will allow for a more comprehensive assessment of the relationship between these regions.

6. CONCLUSIONS

The Warren Inlier is dominated by a Mesoproterozoic S_2 fabric which was deformed in a dominantly E-W to NE-SW principle stress regime during the Delamerian Orogeny. Regional scale fold orientations indicate that this fabric was near horizontal prior to the Delamerian deformation. The only pre-Delamerian fold structures are preserved in early pegmatites, which are believed to be synchronous with the S_2 fabric. Metamorphic monazite and zircon from the early pegmatites suggest that this event occurred at approximately 1570 – 1560 Ma. A metamorphic event is also recorded in the Springfield Sequence at ~ 1580 Ma, which is consistent with previous studies, and is coincident with the Olarian Orogeny in the Curnamona Province to the east. The younger ~1560 Ma ages are consistent with a retrograde metamorphic event also documented in the Curnamona Province (Rutherford *et al.* 2007), and it is likely that these regions share this tectonic history.

The Springfield Sequence to the immediate east of the Warren Inlier has been shown to be an allochthonous basement unit, as opposed to sheared Adelaidean metasediments as they were originally mapped. Detrital zircons from this sequence indicate that deposition of this part of the basement occurred between 1744 Ma and 1625 Ma. This indicates that the Barossa complex was deposited after the Wallaroo Group to the west, and prior to, or synchronous to, the lower Willyama supergroup. This may be indicating either an extension of the Willyama supergroup, or a progressive eastward stepping series of basins was developing on the eastern margin of the Gawler Craton between 1800 Ma and 1600 Ma, the latter of which may be an indication of a retreating subduction margin.

ACKNOWLEDGMENTS

Special thanks go to the project supervisors Alan Collins and Martin Hand for their constructive feedback, expertise, and patience throughout the course of the project. The author is very grateful to Craig Kellond and Edwina Ingham for their valuable assistance in the field. Katie Howard and the staff at Adelaide Microscopy are also thanked for their time and instruction during sample preparation, and during geochronology data collection and analysis.

Matthew Bald, Alex Corrick, Jake McFarlane, Robyn Williamson, and Sonia Surace are thanked for their reviews and feedback of drafts of the manuscript.

SA Water is thanked for access to the Warren Reservoir and South Para River property and for allowing the collection of samples. The owners of the Springfield property and Forestry SA are also thanked for allowing access to their properties and for allowing sample collection.

- ALEINIKOFF J. N., SCHENCK W. S., PLANK M. O., SROGI L., FANNING C. M., KAMO S. L. & BOSBYSELL H. 2006. Deciphering igneous and metamorphic events in high-grade rocks of the Wilmington Complex, Delaware: Morphology, cathodoluminescence and backscattered electron zoning, and SHRIMP U-Pb geochronology of zircon and monazite. *Geological Society of America Bulletin* **118**, 39-64.
- ALLMENDINGER R. W., CARDOZO N. & FISHER D. 2012. *Structural geology algorithms: Vectors and tensors in structural geology*. Cambridge University Press.
- BAROVICH K. & HAND M. 2008. Tectonic setting and provenance of the Paleoproterozoic Willyama Supergroup, Curnamona Province, Australia: Geochemical and Nd isotopic constraints on contrasting source terrain components. *Precambrian Research* **166**, 318-337.
- BELOUSOVA E. A., PREISS W. V., SCHWARZ M. P. & GRIFFIN W. L. 2006. Tectonic affinities of the Houghton Inlier, South Australia: U - Pb and Hf-isotope data from zircons in modern stream sediments. *Australian Journal of Earth Sciences* **53**, 971-989.
- BETTS P. G. & GILES D. 2006. The 1800–1100 Ma tectonic evolution of Australia. *Precambrian Research* **144**, 92-125.
- BETTS P. G., GILES D., FODEN J., SCHAEFER B. F., MARK G., PANKHURST M. J., FORBES C. J., WILLIAMS H. A., CHALMERS N. C. & HILLS Q. 2009. Mesoproterozoic plume-modified orogenesis in eastern Precambrian Australia. *Tectonics* **28**, TC3006.
- BETTS P. G., GILES D. & SCHAEFER B. F. 2008. Comparing 1800–1600 Ma accretionary and basin processes in Australia and Laurentia: Possible geographic connections in Columbia. *Precambrian Research* **166**, 81-92.
- BETTS P. G., GILES D., SCHAEFER B. F. & MARK G. 2007. 1600–1500 Ma hotspot track in eastern Australia: implications for Mesoproterozoic continental reconstructions. *Terra Nova* **19**, 496-501.
- BOGER S. D. 2011. Antarctica — Before and after Gondwana. *Gondwana Research* **19**, 335-371.
- COLLINS W. J. & SHAW R. D. 1995. Geochronological constraints on orogenic events in the Arunta Inlier: a review. *Precambrian Research* **71**, 315-346.

- CONOR C. H. H. 1984. Draft report, Williamstown industrial mineral deposits. Geology of kaolin–sillimanite–muscovite deposits, near Williamstown, Hd. Barossa, Mt. Lofty Ranges, South Aust. *Department of Primary Industries and Resources South Australia*.
- COOPER J. A. & COMPSTON W. 1971. Rb-Sr dating within the Houghton Inlier, South Australia. *Geological Society of South Australia, Journal* **17**, 213-219.
- CREASER R. A. & COOPER J. A. 1993. U-Pb geochronology of middle Proterozoic felsic magmatism surrounding the Olympic Dam Cu-U-Au-Ag and Moonta Cu-Au-Ag deposits, South Australia. *Economic Geology* **88**, 186-197.
- CROWHURST P. V. 1988. The geology, petrology and geochemistry of the Proterozoic inlier, south of Myponga, Fleurieu Peninsula, South Australia. University of Adelaide (unpubl.).
- CUTTS K., HAND M. & KELSEY D. E. 2011. Evidence for early Mesoproterozoic (ca. 1590 Ma) ultrahigh-temperature metamorphism in southern Australia. *Lithos* **124**, 1-16.
- FANNING C. M., FLINT R. B., PARKER A. J., LUDWIG K. R. & BLISSETT A. H. 1988. Refined Proterozoic evolution of the Gawler Craton, South Australia, through U-Pb zircon geochronology. *Precambrian Research* **40–41**, 363-386.
- FANNING C. M., REID A. J. & TEALE G. 2007. *A geochronological framework for the Gawler Craton, South Australia* (Bulletin 55). Geological Survey of South Australia.
- FLINT R. B., BLISSETT A. H., CONOR C. H. H., COWLEY W. M., CROSS K. C., CREASER R. A., DALY S. J., KRIEG G. W., MAJOR R. B., TEALE G. S. & PARKER A. J. 1993. Mesoproterozoic. In: Drexel J. F., Preiss W. V. & Parker A. J. eds., *The Geology of South Australia, Volume 1, The Precambrian*, pp 107-168, Geological Survey of South Australia, Adelaide.
- FODEN J., ELBURG M. A., DOUGHERTY-PAGE J. & BURTT A. 2006. The timing and duration of the Delamerian orogeny: Correlation with the Ross Orogen and implications for Gondwana assembly. *Journal of Geology* **114**, 189-210.
- FORBES C. J., BETTS P. G., GILES D. & WEINBERG R. 2008. Reinterpretation of the tectonic context of high-temperature metamorphism in the Broken Hill Block, NSW, and implications on the Palaeo- to Meso-Proterozoic evolution. *Precambrian Research* **166**, 338-349.

- FORBES C. J., GILES D., HAND M., BETTS P. G., SUZUKI K., CHALMERS N. & DUTCH R. 2011. Using P–T paths to interpret the tectonothermal setting of prograde metamorphism: An example from the northeastern Gawler Craton, South Australia. *Precambrian Research* **185**, 65-85.
- FORBES C. J., GILES D., JOURDAN F., SATO K., OMORI S. & BUNCH M. 2012. Cooling and exhumation history of the northeastern Gawler Craton, South Australia. *Precambrian Research* **200–203**, 209-238.
- GILES D., BETTS P. G. & LISTER G. S. 2004. 1.8-1.5-Ga links between the North and South Australian Cratons and the Early-Middle Proterozoic configuration of Australia. *Tectonophysics* **380**, 27-41.
- HAND M., REID A. & JAGODZINSKI L. 2007. Tectonic framework and evolution of the Gawler craton, Southern Australia. *Economic Geology* **102**, 1377-1395.
- IRELAND T. R., FLOTTMANN T., FANNING C. A., GIBSON G. M. & PREISS W. V. 1998. Development of the early Paleozoic Pacific margin of Gondwana from detrital-zircon ages across the Delamerian orogen. *Geology* **26**, 243-246.
- JACKSON S. E., PEARSON N. J., GRIFFIN W. L. & BELOUSOVA E. A. 2004. The application of laser ablation-inductively coupled plasma-mass spectrometry to in situ U–Pb zircon geochronology. *Chemical Geology* **211**, 47-69.
- MANCKTELOW N. S. 1990. The structure of the southern Adelaide Fold Belt, South Australia. In: Jago J. B. & Moore P. J. eds., *The evolution of a Late Precambrian-Early Paleozoic Rift Complex: The Adelaide Geosyncline*, pp 483-495, The Geological Society of Australia Special Publication
- MEERT J. G. 2012. What's in a name? The Columbia (Paleopangaea/Nuna) supercontinent. *Gondwana Research* **21**, 987-993.
- MILLS K. J. 1963. The Geology of the Mount Crawford Granite Gneiss and Adjacent Metasediments. *Transactions of the Royal Society of South Australia* **87**, 167-183.
- MILLS K. J. 1973. The structural geology of the Warren National Park and the western portion of the Mount Crawford State Forest, South Australia. *Transactions of the Royal Society of South Australia* **97**, Pages: 281-315.
- OFFLER R. & FLEMING P. D. 1968. A synthesis of folding and metamorphism in the Mt Lofty Ranges, South Australia. *Journal of the Geological Society of Australia* **15**, 245-266.

- OLIVER N. H. S. & ZAKOWSKI S. 1995. Timing and geometry of deformation, low-pressure metamorphism and anatexis in the eastern Mt Lofty Ranges: The possible role of extension. *Australian Journal of Earth Sciences* **42**, 501-507.
- PAGE R. W., CONOR C. H. H., STEVENS B. P. J., GIBSON G. M., PREISS W. V. & SOUTHGATE P. N. 2005. Correlation of Olary and Broken Hill Domains, Curnamona Province: Possible relationship to Mount Isa and other North Australian Pb-Zn-Ag-bearing successions. *Economic Geology* **100**, 663-676.
- PARKER A. J., DALY S. J., FLINT R. B., FLINT D. J., PREISS W. V. & TEALE G. S. 1993. Paleoproterozoic. In: Drexel J. F., Preiss W. V. & Parker A. J. eds., *The Geology of South Australia, Volume 1: The Precambrian*, pp 51-106, Geological Survey of South Australia, Adelaide.
- PAYNE J. L., HAND M., BAROVICH K., REID A. & EVANS D. A. D. 2009. Correlations and Reconstruction Models for the 2500-1500 Ma evolution of the Mawson Continent. In: Reddy S. M., Mazumder R., Evans D. A. D. & Collins A. S. eds., *Paleoproterozoic Supercontinents and Global Evolution*, Vol. Special Publications, pp 319-357, Geological Society, London.
- PAYNE J. L., HAND M., BAROVICH K. M. & WADE B. P. 2008. Temporal constraints on the timing of high-grade metamorphism in the northern Gawler Craton: implications for assembly of the Australian Proterozoic. *Australian Journal of Earth Sciences* **55**, 623-640.
- PREISS W. V. 1993. Basement inliers of the Mount Lofty Ranges. In: Drexel J. F., Preiss W. V. & Parker A. J. eds., *The geology of South Australia, Volume 1, The Precambrian*, pp 102-105, Geological Survey of South Australia, Adelaide.
- PREISS W. V. 2000. The Adelaide Geosyncline of South Australia and its significance in Neoproterozoic continental reconstruction. *Precambrian Research* **100**, 21-63.
- PREISS W. V., FANNING C. A., SZPUNAR M. A. & BURTT A. C. 2008. Age and tectonic significance of the Mount Crawford Granite Gneiss and a related intrusive in the Oakbank Inlier, Mount Lofty Ranges, South Australia. *MESA Journal* **49**, 38-49.
- RAETZ M., KRABBENDAM M. & DONAGHY A. G. 2002. Compilation of Pb zircon data from the Willyama Supergroup, Broken Hill region, Australia: Evidence for three tectonostratigraphic successions and four magmatic events? *Australian Journal of Earth Sciences* **49**, 965-983.

- RINGENBERGS W. H. 1975. The Petrology, Genesis, and Alteration of Aluminosilicate Bearing Schists and Gneisses at Springfield, Near Williamstown, South Australia. Bsc (Hons) thesis, University of Adelaide (unpubl.).
- RUTHERFORD L., HAND M. & BAROVICH K. 2007. Timing of Proterozoic metamorphism in the southern Curnamona Province: implications for tectonic models and continental reconstructions. *Australian Journal of Earth Sciences* **54**, 65-81.
- SANDIFORD M., ERASER G., ARNOLD J., FODEN J. & FARROW T. 1995. Some causes and consequences of high-temperature, low-pressure metamorphism in the eastern Mt Lofty Ranges, South Australia. *Australian Journal of Earth Sciences* **42**, 233-240.
- SLÁMA J., KOŠLER J., CONDON D. J., CROWLEY J. L., GERDES A., HANCHAR J. M., HORSTWOOD M. S. A., MORRIS G. A., NASDALA L., NORBERG N., SCHALTEGGER U., SCHOENE B., TUBRETT M. N. & WHITEHOUSE M. J. 2008. Plešovice zircon — A new natural reference material for U–Pb and Hf isotopic microanalysis. *Chemical Geology* **249**, 1-35.
- SWAIN G., WOODHOUSE A., HAND M., BAROVICH K., SCHWARZ M. & FANNING C. M. 2005. Provenance and tectonic development of the late Archaean Gawler Craton, Australia; U-Pb zircon, geochemical and Sm-Nd isotopic implications. *Precambrian Research* **141**, 106-136.
- SZPUNAR M., WADE B., HAND M. P. & BAROVICH K. M. 2007. Timing of Proterozoic high-grade metamorphism in the Barossa Complex, southern South Australia; exploring the extent of the 1590 Ma event. *MESA Journal* **47**, 21-27.
- TALBOT J. L. 1963. Retrograde Metamorphism of the Houghton Complex, South Australia. *Transactions of the Royal Society of South Australia* **87**, 185-197.
- WADE B. P., BAROVICH K. M., HAND M., SCRIMGEOUR I. R. & CLOSE D. F. 2006. Evidence for Early Mesoproterozoic Arc Magmatism in the Musgrave Block, Central Australia: Implications for Proterozoic Crustal Growth and Tectonic Reconstructions of Australia. *The Journal of Geology* **114**, 43-63.
- WIEDENBECK M., ALLÉ P., CORFU F., GRIFFIN W. L., MEIER M., OBERLI F., QUADT A. V., RODDICK J. C. & SPIEGEL W. 1995. Three natural zircon standards for U-Th-Pb, Lu-Hf, trace element and REE analyses. *Geostandards Newsletter* **19**, 1-23.
- ZHANG S., LI Z.-X., EVANS D. A. D., WU H., LI H. & DONG J. 2012. Pre-Rodinia supercontinent Nuna shaping up: A global synthesis with new paleomagnetic results from North China. *Earth and Planetary Science Letters* **353–354**, 145-155.

ZHAO G., SUN M., WILDE S. A. & LI S. 2004. A Paleo-Mesoproterozoic supercontinent: assembly, growth and breakup. *Earth-Science Reviews* **67**, 91-123.

Appendix A: LA-ICP-MS raw data for monazites from sample KM12-05

Sample Number	Pb207/U235 - isotope ratios	Pb207/U23 5- 1 σ	Pb206/U238 - isotope ratios	Pb206/U23 8- 1 σ	Rho	Pb207/P b206- ages	Pb207/P b206- 1 σ	Pb206/U 238- ages	Pb206/U 238 - 1 σ	Conc %
05M-S1	0.60697	0.00985	0.07751	0.00126	0.998289	481.9	23.71	481.3	7.55	99.87549
05M-S2	1.21041	0.01997	0.1255	0.00205	0.990067	926.1	22.88	762.2	11.72	82.30213
05M-S3	2.72501	0.04582	0.12039	0.00198	0.97811	2498.3	20.05	732.8	11.42	29.33195
05M-S4	0.63246	0.01027	0.07995	0.00129	0.993651	504.6	23.86	495.8	7.72	98.25604
05M-S5	0.62133	0.01084	0.07882	0.00129	0.938094	496.7	28.32	489.1	7.68	98.4699
05M-S6	0.61712	0.01015	0.07973	0.00129	0.98372	456.7	24.56	494.5	7.68	108.2768
05M-S7	0.62101	0.01123	0.07893	0.00129	0.903788	492.5	30.63	489.7	7.7	99.43147
05M-S8	0.61243	0.01053	0.07932	0.00128	0.938546	451.1	27.35	492.1	7.66	109.0889
05M-S9	0.59837	0.01087	0.07715	0.00126	0.899031	460.6	31.03	479.1	7.51	104.0165
05M-S10	0.64031	0.01084	0.08147	0.00131	0.949805	490.1	27.2	504.9	7.81	103.0198
05M-S11	0.64932	0.01143	0.0849	0.00138	0.923387	432.4	29.09	525.3	8.18	121.4847
05M-S12	0.60401	0.00965	0.07603	0.00122	0.995654	516.3	23.4	472.4	7.3	91.49719
05M-S13	0.63541	0.01024	0.08397	0.00135	0.997617	408.8	24.47	519.8	8.01	127.1526
05M-S14	0.62245	0.01117	0.08099	0.00132	0.908226	443.1	30.21	502	7.86	113.2927
05M-S15	0.61335	0.01021	0.08082	0.0013	0.966289	415.1	26.32	501	7.77	120.6938
05M-S16	1.17452	0.01985	0.10751	0.00174	0.957636	1179.1	24.42	658.3	10.14	55.83072
05M-S17	0.64132	0.01052	0.08226	0.00132	0.978237	474.4	25.72	509.6	7.89	107.4199
05M-S18	0.64487	0.01106	0.0825	0.00134	0.947039	480.2	28.28	511	7.96	106.414
05M-S19	0.60651	0.01024	0.08028	0.0013	0.959122	405.2	27.21	497.8	7.74	122.8529
05M-S20	0.63129	0.01022	0.08096	0.0013	0.991861	474.5	25.04	501.9	7.77	105.7745
05M-S21	0.66376	0.01067	0.08423	0.00133	0.982271	498	25.26	521.3	7.93	104.6787
05M-S22	0.61635	0.00973	0.08008	0.00126	0.996692	446.1	23.78	496.6	7.54	111.3203
05M-S23	0.64636	0.01023	0.08163	0.00129	0.998479	508.6	24.04	505.9	7.66	99.46913
05M-S24	0.57783	0.00999	0.07477	0.00119	0.920564	455.1	28.9	464.8	7.14	102.1314

05M-S25	0.62283	0.01054	0.08042	0.00127	0.933187	459.4	28.18	498.6	7.6	108.5329
05M-S26	0.57718	0.01036	0.07565	0.00121	0.891103	426.8	31.38	470.1	7.23	110.1453
05M-S27	0.60525	0.00992	0.07902	0.00124	0.957432	435.4	26.02	490.3	7.42	112.6091
05M-S28	0.59705	0.00988	0.07768	0.00122	0.949083	443.3	26.59	482.2	7.31	108.7751
05M-S29	0.59495	0.01007	0.07767	0.00122	0.92802	435.7	27.84	482.2	7.32	110.6725
05M-S30	0.60788	0.01028	0.07762	0.00122	0.929418	484.7	28.42	481.9	7.3	99.42232
KM05M2-1	0.63716	0.01121	0.08101	0.00123	0.862997	494.1	31.99	502.1	7.31	101.6191
KM05M2-2	0.6193	0.01119	0.07917	0.0012	0.838864	481.9	33.49	491.2	7.19	101.9299
KM05M2-3	0.59682	0.01091	0.07662	0.00117	0.835338	472.4	34.08	475.9	6.99	100.7409
KM05M2-4	0.61781	0.01165	0.07872	0.00121	0.815135	489.3	35.6	488.5	7.21	99.8365
KM05M2-5	0.61018	0.01171	0.07772	0.0012	0.804543	489.9	36.47	482.5	7.15	98.48949
KM05M2-6	0.61172	0.01151	0.07761	0.00119	0.814904	498.8	35.07	481.8	7.12	96.59182
KM05M2-7	0.5357	0.00868	0.06919	0.00103	0.918747	459.1	27.71	431.3	6.24	93.94467
KM05M2-8	0.60071	0.00946	0.07677	0.00114	0.942946	482.6	26.26	476.8	6.85	98.79818
KM05M2-9	0.59803	0.01081	0.07653	0.00116	0.83854	479.6	33.36	475.4	6.98	99.12427
KM05M2-10	0.61883	0.0107	0.07847	0.00119	0.877063	500	30.7	487	7.09	97.4
KM05M2-11	0.64119	0.011	0.08169	0.00123	0.877668	489.4	30.62	506.2	7.35	103.4328
KM05M2-12	0.63745	0.01175	0.08063	0.00123	0.827593	505.3	33.62	499.9	7.35	98.93133
KM05M2-13	0.62035	0.01154	0.079	0.00121	0.823359	490.1	34.54	490.1	7.21	100
KM05M2-14	3.67822	0.05712	0.27469	0.00409	0.958804	1570.2	21.22	1564.6	20.68	99.64336
KM05M2-15	0.6076	0.01088	0.07806	0.00118	0.844194	470.4	32.63	484.5	7.08	102.9974
KM05M2-16	0.61497	0.01236	0.07863	0.00122	0.771982	480.9	38.94	488	7.28	101.4764
KM05M2-17	3.23751	0.05209	0.24391	0.00365	0.930079	1553.7	22.9	1407	18.92	90.55802
KM05M2-18	0.6222	0.01134	0.07937	0.0012	0.829549	486.1	33.64	492.4	7.2	101.296
KM05M2-19	0.56994	0.00988	0.07387	0.00111	0.866816	451.3	30.49	459.4	6.67	101.7948
KM05M2-20	3.68604	0.05913	0.27212	0.00406	0.930074	1591.8	22.68	1551.5	20.56	97.46827
KM05M2-21	0.64011	0.01099	0.07864	0.00118	0.873968	569.2	29.81	488	7.05	85.73436

KM05M2-22	0.63306	0.01146	0.07889	0.00119	0.833269	537.6	33.28	489.5	7.13	91.05283
KM05M2-23	0.60617	0.01032	0.07727	0.00116	0.881783	487.7	30.19	479.8	6.92	98.38015
KM05M2-24	0.58654	0.00958	0.07451	0.00111	0.912096	495.5	28.01	463.2	6.64	93.48133
KM05M2-25	0.64391	0.01219	0.08215	0.00125	0.803755	486	36.82	508.9	7.44	104.7119
KM05M2-26	0.60249	0.01163	0.07797	0.00119	0.79066	454.7	37.42	484	7.11	106.4438
KM05M2-27	0.79963	0.01728	0.09289	0.00146	0.727326	689.8	42.23	572.6	8.59	83.00957
KM05M2-28	0.59496	0.01285	0.07624	0.00119	0.722684	475.9	44.22	473.7	7.11	99.53772
KM05M2-29	0.59738	0.0111	0.07732	0.00117	0.81437	454.2	35.7	480.1	6.98	105.7023
KM05M2-30	0.60401	0.01142	0.07887	0.00119	0.798019	434.5	36.63	489.4	7.12	112.6352
KM05M2-31	0.61304	0.01222	0.07803	0.00119	0.765073	490.7	39.73	484.4	7.12	98.71612
KM05M2-32	0.59446	0.01122	0.07655	0.00115	0.795944	465	37.25	475.5	6.91	102.2581
05Z-S1	0.64149	0.01193	0.08125	0.00133	0.880193	502.2	32.16	503.6	7.95	100.2788
05Z-S2	0.6353	0.01076	0.08323	0.00135	0.95768	427.8	27.17	515.4	8.01	120.4769
05Z-S3	0.62848	0.01065	0.08061	0.00131	0.959012	474.3	27.24	499.8	7.79	105.3763
05Z-S4	0.60354	0.01032	0.079	0.00128	0.947565	429.5	27.6	490.2	7.66	114.1327
05Z-S5	0.61684	0.01014	0.07954	0.00129	0.986595	462.3	25.36	493.4	7.67	106.7272
05Z-S6	0.61407	0.01061	0.08037	0.00131	0.943365	429.9	28.05	498.3	7.8	115.9107
05Z-S7	0.60207	0.01033	0.07927	0.00129	0.948479	416.7	27.57	491.8	7.7	118.0226
05Z-S8	3.71305	0.0598	0.27899	0.00451	0.996282	1558.9	20.24	1586.3	22.75	101.7576
05Z-S9	0.644	0.01163	0.08437	0.00138	0.905727	427.6	30.41	522.2	8.23	122.1235
05Z-S10	0.61649	0.01028	0.08068	0.00131	0.97373	429.9	25.77	500.2	7.82	116.3526
05Z-S11	0.62571	0.01066	0.08083	0.00131	0.951294	458.8	26.61	501.1	7.83	109.2197
05Z-S12	0.61373	0.01047	0.08083	0.00131	0.950013	416.1	26.97	501.1	7.83	120.4278
05Z-S13	0.61264	0.01059	0.07871	0.00128	0.940783	470.6	27.93	488.4	7.65	103.7824
05Z-S14	0.59054	0.00992	0.07754	0.00126	0.967347	422.8	26.16	481.4	7.51	113.86
05Z-S16	1.29063	0.02107	0.12467	0.00201	0.987578	1071.8	22.27	757.4	11.54	70.66617
05Z-S17	0.64745	0.01162	0.08186	0.00134	0.91208	506.2	29.59	507.2	7.97	100.1976
05Z-S18	0.60419	0.01075	0.07848	0.00128	0.916676	446.8	29.13	487	7.65	108.9973

05Z-S19	0.6158	0.01109	0.07905	0.00129	0.906141		472.4	30.38	490.5	7.71		103.8315
05Z-S20	0.6156	0.01024	0.08112	0.00131	0.970827		415	25.61	502.8	7.81		121.1566

Appendix B: LA-ICP-MS raw data for monazite analyses for sample KM12-08

Sample Number	Pb207/U235 - isotope ratios	Pb207/U23 5- 1 σ	Pb206/U238 - isotope ratios	Pb206/U23 8- 1 σ	Rho	Pb207/P b206- ages	Pb207/P b206- 1 σ	Pb206/U 238- ages	Pb206/U 238 - 1 σ	Conc %
08M-S1	0.58632	0.00896	0.07878	0.00125	0.963117	371	23.79	488.8	7.44	131.752
08M-S2	3.43551	0.05171	0.26693	0.00422	0.952069	1495.8	19.24	1525.2	21.46	101.9655
08M-S3	0.59575	0.00945	0.07664	0.00122	0.996468	467.7	25.47	476	7.29	101.7746
08M-S4	3.46721	0.05241	0.27019	0.00427	0.956479	1490.2	19.48	1541.8	21.68	103.4626
08M-S5	0.56297	0.01118	0.07438	0.00122	0.825937	408.8	37.42	462.5	7.32	113.136
08M-S6	3.48573	0.05289	0.26928	0.00426	0.959123	1506.7	19.65	1537.1	21.63	102.0177
08M-S7	3.45139	0.05315	0.27402	0.00435	0.970068	1454.7	20.5	1561.2	21.99	107.3211
08M-S8	3.47444	0.05385	0.27911	0.00443	0.976501	1432.3	20.86	1586.9	22.33	110.7938
08M-S9	3.59938	0.055	0.27419	0.00434	0.965377	1533.1	19.94	1562	21.95	101.8851
08M-S10	3.31659	0.05132	0.26656	0.00423	0.975101	1431.4	20.8	1523.3	21.51	106.4203
08M-S11	3.34342	0.05163	0.26062	0.00413	0.974471	1489.7	20.58	1493	21.1	100.2215
08M-S12	3.53071	0.05248	0.27462	0.00431	0.94708	1493.8	18.79	1564.2	21.8	104.7128
08M-S13	3.32151	0.05125	0.26471	0.00418	0.97713	1447.5	20.73	1513.9	21.33	104.5872
08M-S14	0.61921	0.0109	0.08007	0.00128	0.908137	456.4	30.77	496.6	7.66	108.8081
08M-S15	3.59861	0.05383	0.27363	0.00429	0.954105	1536.5	19.12	1559.2	21.72	101.4774
08M-S16	3.71388	0.05558	0.27942	0.00438	0.954716	1556.4	19.13	1588.4	22.07	102.056
08M-S17	3.34157	0.05224	0.25414	0.00402	0.988325	1536	21.28	1459.8	20.66	95.03906
08M-S18	3.31475	0.05083	0.26558	0.00418	0.97429	1437.2	20.66	1518.3	21.28	105.6429
08M-S19	2.17357	0.03595	0.18531	0.00296	0.965756	1317.7	24.69	1095.9	16.08	83.16764
08M-S20	1.02543	0.02081	0.11383	0.00187	0.809504	785.9	37.01	694.9	10.85	88.42092
08M-S21	1.0771	0.01807	0.1111	0.00175	0.938905	938.3	26.74	679.1	10.16	72.37557
08M-S22	3.39915	0.05155	0.26421	0.0041	0.977291	1494.8	20.14	1511.3	20.9	101.1038
08M-S23	0.59446	0.01294	0.07541	0.00123	0.749315	498.3	42.44	468.7	7.39	94.0598
08M-S24	0.61338	0.01378	0.07699	0.00127	0.73426	522.1	44.43	478.1	7.59	91.5725

08M-S25	3.40877	0.053	0.26578	0.00413	0.999424	1488.9	21.24	1519.4	21.01	102.0485
08M-S26	3.25042	0.05078	0.24855	0.00386	0.994078	1525.7	21.34	1431	19.91	93.79301
08M-S27	3.62752	0.05624	0.27627	0.00427	0.996916	1533.3	20.94	1572.6	21.58	102.5631
08M-S28	3.39298	0.0541	0.26266	0.00408	0.974205	1502.6	22.3	1503.4	20.83	100.0532
08M-S29	3.40053	0.05432	0.26077	0.00405	0.972264	1520.4	22.32	1493.8	20.69	98.25046
08M-S30	0.6541	0.01057	0.08147	0.00126	0.957066	538.7	26.96	504.9	7.5	93.72564
08Z-S1	0.58171	0.0104	0.0805	0.00137	0.951914	304.4	30.4	499.1	8.19	163.9619
08Z-S2	3.08056	0.05065	0.25134	0.00426	0.970067	1402.7	21.55	1445.4	21.94	103.0441
08Z-S3	0.57851	0.01304	0.0778	0.00138	0.786924	369.2	44.11	483	8.24	130.8234
08Z-S4	0.6573	0.01306	0.08362	0.00145	0.872727	492.5	35.95	517.7	8.62	105.1168
08Z-S5	0.8193	0.0169	0.10097	0.00176	0.845039	562.6	37.52	620.1	10.32	110.2204
08Z-S6	3.39888	0.05495	0.27333	0.0046	0.960641	1430.3	20.79	1557.7	23.27	108.9072
08Z-S7	3.23794	0.05271	0.26346	0.00443	0.968133	1407.9	21.24	1507.5	22.61	107.0744
08Z-S8	0.56698	0.00982	0.07909	0.00134	0.978227	286.2	29.03	490.7	7.99	171.4535
08Z-S9	0.53656	0.00942	0.07524	0.00127	0.96144	274.2	29.95	467.6	7.63	170.5325
08Z-S10	3.54827	0.05866	0.27972	0.0047	0.9839	1468.1	22.14	1590	23.69	108.3032
08Z-S11	2.84185	0.04669	0.22997	0.0039	0.968789	1418.3	21.34	1334.3	20.42	94.07742
08Z-S12	1.15268	0.02225	0.11858	0.00206	0.899983	943.9	31.7	722.4	11.87	76.53353
08Z-S13	3.45342	0.05589	0.26422	0.00445	0.960927	1524.9	20.44	1511.4	22.71	99.1147
08Z-S14	3.56244	0.0568	0.28084	0.00471	0.95069	1468.2	20	1595.6	23.72	108.6773
08Z-S15	1.56977	0.02601	0.14526	0.00245	0.982391	1157.5	22.93	874.3	13.79	75.53348
08Z-S16	3.51317	0.05642	0.27639	0.00463	0.958683	1472.1	20.53	1573.2	23.4	106.8677
08Z-S17	0.56426	0.00962	0.07867	0.00133	0.991623	287.4	28.14	488.2	7.92	169.8678
08Z-S18	1.28346	0.0226	0.1317	0.00224	0.965909	949.3	27.11	797.6	12.73	84.0198
08Z-S19	0.59703	0.01235	0.07909	0.00137	0.837391	403	38.59	490.7	8.19	121.7618
08Z-S20	3.28079	0.05526	0.26666	0.00449	0.999669	1410.1	23.29	1523.8	22.85	108.0633

Appendix C: LA-ICP-MS Raw data for analyses on zircon grains from sample KM12-01

Sample Number	Pb207/U235 - isotope ratios	Pb207/U23 5- 1 σ	Pb206/U238 - isotope ratios	Pb206/U23 8- 1 σ	Rho	Pb207/P b206- ages	Pb207/P b206- 1 σ	Pb206/U 238- ages	Pb206/U 238 - 1 σ	Conc %
KM0101	0.57796	0.01022	0.07252	0.00104	0.811003	522	34.02	451.3	6.22	86
KM0102	2.59183	0.03979	0.17921	0.0025	0.908679	1712.4	22.86	1062.6	13.68	62
KM0103	0.56209	0.0105	0.07216	0.00104	0.771531	471.1	37.07	449.2	6.26	95
KM0104	3.67899	0.05695	0.27072	0.00379	0.904386	1597.1	23.48	1544.4	19.24	97
KM0105	3.72082	0.05766	0.27671	0.00388	0.904838	1577.3	23.56	1574.8	19.58	100
KM0106	3.57326	0.05559	0.26622	0.00374	0.903023	1573.9	23.7	1521.6	19.02	97
KM0107	0.71986	0.01166	0.08479	0.0012	0.873748	659.4	28.9	524.6	7.12	80
KM0108	3.61331	0.05683	0.26888	0.00378	0.893842	1576.1	24.08	1535.1	19.23	97
KM0109	3.21074	0.05076	0.24212	0.00341	0.890855	1551.2	24.34	1397.7	17.71	90
KM0110	3.146	0.05094	0.23645	0.00335	0.874994	1557.5	25.29	1368.2	17.48	88
KM0111	3.39135	0.05425	0.25174	0.00356	0.884037	1580.8	24.67	1447.4	18.32	92
KM112	3.43247	0.0517	0.25717	0.00356	0.919064	1563.5	22.91	1475.3	18.23	94
KM113	3.05066	0.04777	0.2284	0.00319	0.891935	1564.8	24.39	1326.1	16.76	85
KM114	0.71577	0.01138	0.08288	0.00116	0.880318	695.9	28.21	513.3	6.9	74
KM115	1.75762	0.02725	0.1529	0.00214	0.902744	1277.7	24.86	917.2	11.94	72
KM116	3.44602	0.0536	0.25601	0.00358	0.89904	1579.2	23.81	1469.4	18.39	93
KM117	3.59894	0.05666	0.27121	0.00381	0.892313	1552.4	24.29	1546.9	19.32	100
KM118	3.18429	0.05081	0.23875	0.00337	0.884606	1561.9	24.72	1380.2	17.52	88
KM119	2.64011	0.04292	0.10491	0.00149	0.873638	2675.7	22.48	643.1	8.7	24
KM120	0.60585	0.01225	0.07435	0.0011	0.731713	570.6	39.99	462.3	6.6	81
KM121	2.66058	0.04461	0.17297	0.00248	0.855116	1824.8	25.61	1028.5	13.61	56
KM122	3.47071	0.05868	0.26193	0.00376	0.849045	1549.6	26.74	1499.7	19.19	97
KM123	3.34071	0.05762	0.24773	0.00357	0.835517	1582.5	27.35	1426.7	18.46	90

KM124	3.27561	0.06104	0.24368	0.00359	0.790592		1576.5	30.23	1405.8	18.62		89
KM125	0.6101	0.01257	0.07675	0.00116	0.733576		516.1	40.85	476.7	6.92		92

Appendix D: LA-ICP-MS Raw data for analyses on zircon grains from sample KM12-07

Sample Number	Pb207/U235 - isotope ratios	Pb207/U23 5- 1 σ	Pb206/U238 - isotope ratios	Pb206/U23 8- 1 σ	Rho	Pb207/P b206- ages	Pb207/P b206- 1 σ	Pb206/U 238- ages	Pb206/U 238 - 1 σ	Conc %
KM071	3.44279	0.05328	0.2581	0.00362	0.906289	1562.4	23.5	1480.1	18.65	94.73246
KM072	2.82203	0.04443	0.2226	0.00314	0.895962	1466.2	24.54	1295.6	16.62	88.36448
KM073	3.49585	0.05514	0.26309	0.00372	0.896447	1555	24.13	1505.6	19	96.82315
KM074	2.64839	0.04229	0.19534	0.00278	0.891247	1592.7	24.43	1150.2	14.93	72.21699
KM075	2.09168	0.03398	0.18056	0.00258	0.879569	1292.8	26.07	1070.1	13.99	82.77382
KM076	3.8713	0.06446	0.28906	0.00416	0.864315	1569.8	26.04	1636.8	20.59	104.2681
KM077	3.49464	0.05864	0.26433	0.00381	0.858988	1545.5	26.33	1511.9	19.15	97.82595
KM078	0.91829	0.01612	0.09351	0.00136	0.828506	963.9	30.57	576.2	7.89	59.77799
KM079	3.04542	0.05383	0.23239	0.0034	0.827722	1529	28.38	1347	17.36	88.0968
KM0710	3.07493	0.05612	0.23213	0.00343	0.809618	1549.2	29.59	1345.7	17.42	86.86419
KM0711	3.29854	0.05252	0.24933	0.00359	0.904309	1547	24.09	1435	18.46	92.76018
KM0712	3.6161	0.05765	0.27229	0.00392	0.903016	1554.1	24.05	1552.4	19.79	99.89061
KM0713	2.88569	0.04657	0.22206	0.00321	0.895732	1513.3	24.62	1292.8	16.84	85.42919
KM0714	2.06316	0.03385	0.17415	0.00252	0.881965	1336.7	25.89	1034.9	13.78	77.42201
KM0715	3.60465	0.06017	0.27214	0.00396	0.871738	1549.3	25.76	1551.6	19.92	100.1485
KM0716	3.53618	0.06	0.26579	0.00388	0.860352	1557.6	26.34	1519.4	19.59	97.54751
KM0717	3.36229	0.05838	0.25348	0.00372	0.845221	1552	27.26	1456.4	18.92	93.84021
KM0718	3.15269	0.05613	0.23623	0.00349	0.829806	1563.4	28.22	1367.1	17.93	87.44403
KM0719	1.55694	0.0284	0.1375	0.00204	0.813357	1248.7	30.27	830.5	11.37	66.50917
KM0720	2.29326	0.04323	0.18261	0.00273	0.79306	1448.4	31.03	1081.2	14.6	74.64789
KM0721	3.48892	0.05636	0.26573	0.00388	0.903881	1532.7	24.42	1519.1	19.6	99.11268
KM0722	2.79712	0.04535	0.21946	0.00321	0.90216	1476.5	24.91	1279	16.8	86.62377
KM0723	3.40091	0.05549	0.25973	0.0038	0.896689	1527.6	24.93	1488.5	19.25	97.44043
KM0724	3.3163	0.05504	0.25608	0.00376	0.884683	1506.8	25.75	1469.7	19.08	97.53783

KM0725	2.99052	0.05027	0.23424	0.00344	0.873645	1479.7	26.52	1356.7	17.77	91.6875
KM0726	3.17829	0.05472	0.24212	0.00357	0.856416	1532.3	27.28	1397.7	18.31	91.21582
KM0727	3.54709	0.06191	0.26976	0.00399	0.847436	1535.5	27.87	1539.6	19.95	100.267
KM0728	3.01434	0.05436	0.23257	0.00346	0.824964	1508.3	29.42	1348	17.81	89.37214
KM0729	3.1827	0.05867	0.24128	0.0036	0.809396	1541.5	30.27	1393.3	18.38	90.38599

Appendix E: U-Pb LA-ICP-MS analysis data for sample KM12-11

Sample Number	Pb207/U235 - isotope ratios	Pb207/U23 5- 1 σ	Pb206/U238 - isotope ratios	Pb206/U23 8- 1 σ	Rho	Pb207/P b206- ages	Pb207/P b206- 1 σ	Pb206/U 238- ages	Pb206/U 238 - 1 σ	Conc %
KM11Z1	2.48371	0.04209	0.18252	0.00264	0.853523	1600	27.05	1080.7	14.4	67.54375
KM11Z2	3.5479	0.0547	0.26451	0.00372	0.912189	1573	23.18	1512.9	18.97	96.17928
KM11Z3	3.6003	0.0584	0.26395	0.00376	0.878197	1604.3	25.13	1510	19.19	94.12205
KM11Z4	3.17157	0.05379	0.23685	0.00341	0.848895	1569.9	27.08	1370.3	17.8	87.28581
KM11Z5	3.51827	0.05569	0.25777	0.00364	0.892115	1605.5	24.08	1478.4	18.64	92.08346
KM11Z6	1.60239	0.02764	0.13518	0.00194	0.831993	1337.9	28.65	817.3	11.04	61.08827
KM11Z7	2.11154	0.03394	0.16191	0.00229	0.879932	1520.1	24.93	967.4	12.68	63.64055
KM11Z8	3.32926	0.058	0.24973	0.00361	0.829767	1561.6	28.14	1437.1	18.6	92.02741
KM11Z9	3.63274	0.06171	0.26789	0.00383	0.84163	1593.4	26.93	1530.1	19.48	96.02736
KM11Z10	3.51367	0.06429	0.26	0.0038	0.798781	1587.1	30.09	1489.8	19.45	93.86932
KM11Z11	2.64291	0.04238	0.19705	0.0028	0.886141	1572.7	24.42	1159.5	15.1	73.72671
KM11Z12	3.78484	0.06491	0.27273	0.00396	0.846639	1636.3	26.97	1554.7	20.07	95.01314
KM11Z13	3.65479	0.06434	0.26884	0.00393	0.830386	1598	28.16	1534.9	19.98	96.05131
KM11Z14	3.69453	0.06433	0.27143	0.00395	0.835766	1600.3	27.63	1548	20.04	96.73186
KM11Z15	2.68128	0.04489	0.20838	0.00299	0.857053	1494.6	26.27	1220.2	15.96	81.64057
KM11Z16	2.80469	0.04882	0.21308	0.00309	0.833111	1537.5	27.74	1245.2	16.44	80.98862
KM11Z17	0.58597	0.01245	0.07505	0.00113	0.708653	476.7	43.19	466.5	6.75	97.86029
KM11Z18	3.59432	0.06327	0.26658	0.00388	0.826843	1582.6	27.93	1523.4	19.74	96.25932
KM11Z19	3.91208	0.07074	0.2915	0.00427	0.810088	1573.9	29.06	1649	21.32	104.7716
KM11Z20	3.69124	0.06657	0.27611	0.00404	0.811321	1566.6	28.9	1571.8	20.39	100.3319
KM11Z21	3.73949	0.06326	0.27994	0.00398	0.84043	1565.2	26.43	1591	20.02	101.6484
KM11Z22	3.81994	0.06467	0.28464	0.00404	0.838377	1573.8	26.45	1614.7	20.26	102.5988
KM11Z23	3.09276	0.05097	0.2228	0.00314	0.855157	1636.8	25.23	1296.7	16.57	79.22165
KM11Z24	1.59383	0.02703	0.12813	0.00181	0.832959	1430.2	27.09	777.2	10.34	54.34205

KM11Z25	3.73962	0.06145	0.27866	0.00392	0.856085	1573.8	25.37	1584.6	19.75	100.6862
KM11Z26	1.85337	0.03167	0.15764	0.00222	0.824139	1321.8	27.94	943.6	12.37	71.3875
KM11Z27	3.31016	0.05817	0.246	0.00348	0.804997	1578.8	28.09	1417.8	18.03	89.80238
KM11Z28	3.52578	0.05957	0.26259	0.00369	0.831717	1574.8	26.55	1503.1	18.83	95.44704
KM11Z29	3.25379	0.05594	0.24743	0.00348	0.818077	1535.7	27.42	1425.2	17.98	92.80458
KM11Z30	1.99714	0.03668	0.15618	0.00222	0.773939	1482.7	30.49	935.5	12.35	63.09435

Appendix F: U-Pb LA-ICP-MS analysis data for sample KM12-17

Sample Number	Pb207/U235 - isotope ratios	Pb207/U23 5- 1 σ	Pb206/U238 - isotope ratios	Pb206/U23 8- 1 σ	Rho	Pb207/P b206- ages	Pb207/P b206- 1 σ	Pb206/U 238- ages	Pb206/U 238 - 1 σ	Conc %
KM17Z1	11.55018	0.19826	0.48874	0.00744	0.886847	2571.5	24.07	2565.2	16.04	99.75501
KM17Z2	5.23738	0.09218	0.34374	0.00515	0.851245	1807.9	27.2	1904.6	15.01	105.3487
KM17Z3	5.5661	0.09722	0.35628	0.00531	0.853294	1853.3	26.8	1964.5	15.03	106.0001
KM17Z4	5.27094	0.08973	0.34506	0.00507	0.863105	1812.5	25.92	1911	14.53	105.4345
KM17Z5	7.40809	0.11946	0.41138	0.00592	0.892406	2106.3	23	2221.2	14.43	105.4551
KM17Z6	10.58721	0.18673	0.4375	0.00661	0.856625	2611	25.29	2339.4	16.36	89.59786
KM17Z7	11.53827	0.19542	0.48081	0.00705	0.86574	2597.1	23.79	2530.8	15.83	97.44715
KM17Z8	11.74433	0.19946	0.48725	0.00712	0.8604	2604.4	23.93	2558.8	15.89	98.24912
KM17Z9	10.55686	0.214	0.45053	0.00731	0.800414	2557.3	31.06	2397.6	18.8	93.75513
KM17Z10	4.66297	0.0866	0.30858	0.00459	0.800921	1792.8	29.96	1733.7	15.53	96.70348
KM17Z11	4.7783	0.08021	0.31595	0.0046	0.86733	1794.9	25.75	1769.9	14.1	98.60716
KM17Z12	3.73053	0.07234	0.26678	0.00407	0.786744	1650.9	32.38	1524.4	15.53	92.33751
KM17Z13	4.27323	0.07342	0.31369	0.00456	0.84607	1602.3	27.42	1758.8	14.14	109.7672
KM17Z14	5.4073	0.09214	0.35401	0.00514	0.852079	1812.9	26.45	1953.7	14.6	107.7666
KM17Z15	4.36102	0.07289	0.2964	0.00425	0.857889	1744.7	25.92	1673.4	13.8	95.91334
KM17Z16	8.63526	0.14006	0.42205	0.00598	0.873572	2328.1	23.3	2269.8	14.76	97.49581
KM17Z17	9.65716	0.15929	0.43865	0.00624	0.862437	2452.8	23.67	2344.6	15.18	95.58871
KM17Z18	6.79041	0.11328	0.36926	0.00524	0.850632	2143.4	24.96	2025.9	14.77	94.51806
KM17Z19	7.96312	0.13971	0.39186	0.00569	0.827632	2316.4	26.47	2131.5	15.83	92.01779
KM17Z20	9.97751	0.1695	0.41864	0.00594	0.835215	2586	24.65	2254.3	15.68	87.17324
KM17Z21	11.36126	0.18024	0.45723	0.0065	0.896095	2654.7	21.41	2427.3	14.81	91.43406
KM17Z22	298.0752	67.91415	2.16249	0.57322	1.16341	5236.8	273.96	7422.1	230.57	141.7297
KM17Z23	4.74449	0.08504	0.32001	0.00474	0.826382	1757.8	28.15	1789.8	15.03	101.8205
KM17Z24	3.88625	0.0755	0.2618	0.004	0.786455	1760.1	31.52	1499	15.69	85.16562

KM17Z25	3.89035	0.06938	0.2243	0.00332	0.829972		2039.9	26.8	1304.6	14.4	63.95412
KM17Z26	13.1079	0.23621	0.53283	0.008	0.833175		2638.1	25.3	2753.4	17	104.3706
KM17Z27	3.80545	0.0716	0.237	0.00358	0.802838		1902.4	29.07	1371.1	15.13	72.07212

Appendix G:
Thorium Uranium ratios for Sample
KM12-11

Analysis #	Pb ²⁰⁷ /Pb ²⁰⁶ Age	Th/U Ratio
KM11Z1	1600	0.0456
KM11Z2	1573	0.0146
KM11Z3	1604.3	0.0441
KM11Z4	1569.9	0.1603
KM11Z5	1605.5	0.6976
KM11Z6	1337.9	0.0846
KM11Z7	1520.1	0.0158
KM11Z8	1561.6	0.1497
KM11Z9	1593.4	0.0238
KM11Z10	1587.1	0.0248
KM11Z11	1572.7	0.1357
KM11Z12	1636.3	0.2307
KM11Z13	1598	0.0354
KM11Z14	1600.3	0.204
KM11Z15	1494.6	0.1743
KM11Z16	1537.5	0.1437
KM11Z17	476.7	0.1126
KM11Z18	1582.6	0.0148
KM11Z19	1573.9	0.0246
KM11Z20	1566.6	0.0248
KM11Z21	1565.2	0.0259
KM11Z22	1573.8	1.0908
KM11Z23	1636.8	0.0113
KM11Z24	1430.2	0.3784
KM11Z25	1573.8	0.0132
KM11Z26	1321.8	0.1445
KM11Z27	1578.8	0.1707
KM11Z28	1574.8	0.387
KM11Z29	1535.7	0.0226
KM11Z30	1482.7	0.0251

Appendix H:
Thorium Uranium ratios for sample
KM12-17

Analysis #	Pb ²⁰⁷ /Pb ²⁰⁶ Age	Th/U Ratio
KM17Z1	2571.5	0.672143
KM17Z2	1807.9	0.372666
KM17Z3	1853.3	0.546699
KM17Z4	1812.5	0.809219
KM17Z5	2106.3	0.993864
KM17Z6	2611	0.596012
KM17Z7	2597.1	0.548635
KM17Z8	2604.4	0.505716
KM17Z9	2557.3	0.693185
KM17Z10	1792.8	0.251807
KM17Z11	1794.9	0.280514
KM17Z12	1650.9	0.098362
KM17Z13	1602.3	0.074878
KM17Z14	1812.9	0.260029
KM17Z15	1744.7	0.20244
KM17Z16	2328.1	0.241674
KM17Z17	2452.8	0.249272
KM17Z18	2143.4	0.359669
KM17Z19	2316.4	0.394333
KM17Z20	2586	0.686803
KM17Z21	2654.7	0.725424
KM17Z23	1757.8	0.320923
KM17Z24	1760.1	0.299605
KM17Z25	2039.9	0.164316
KM17Z26	2638.1	0.597443
KM17Z27	1902.4	0.125276